Marine Structures 78 (2021) 102985

Contents lists available at ScienceDirect

Marine Structures

journal homepage: www.elsevier.com/locate/marstruc

Algorithmic formulation of clay and sand pipe–soil interaction models for on-bottom stability analysis

Vegard Longva [a,*], Guomin Ji [b], Svein Sævik [c], Naiquan Ye [a], Janne K.Ø. Gjøsteen [a], Egil Giertsen [a], Yanbin Wang [d]

[a] SINTEF Ocean, Postbox 4762 Torgarden, 7465 Trondheim, Norway
[b] Department of Manufacturing and Civil Engineering, Norwegian University of Science and Technology, 2821 Gjøvik, Norway
[c] Department of Marine Technology, Norwegian University of Science and Technology, 7491 Trondheim, Norway
[d] China University of Petroleum, Beijing, 18 Fuxue Road, Changping District, Beijing, 102249, China

ARTICLE INFO

Keywords:
Pipe–soil interaction
On-bottom stability
Elasto-plastic
Algorithmic optimization
Backward-Euler update algorithm

ABSTRACT

This paper presents a new algorithmic formulation of the clay and sand pipe–soil interaction models recommended by the DNV-RP-F109 code for dynamic on-bottom stability analysis of submarine pipelines. The pipe–soil force update algorithm is formulated within the framework of computational elasto-plasticity and applies Backward-Euler integration to ensure stability and robustness for large time step sizes. Algorithmic optimization techniques are developed by utilizing a closed-form solution and subincrementation. A numerical verification study covering full cyclic displacement ranges of a 12 inch pipeline is presented. The new formulation is shown to increase the time step size by a factor of up to 50 compared to commercial software tools for on-bottom stability analysis. This achievement will be particularly beneficial for long-duration 3D nonlinear time domain on-bottom stability analysis.

1. Introduction

For any pipeline, umbilical, power cable or flexible a major design challenge is to ensure that the product remains on the seabed where it was installed without excessive lateral displacements. Such design is called on-bottom stability, which involves determining a submerged weight capable of withstanding hydrodynamic loading through friction and passive soil resistance. Alternatively, on-bottom stability can be ensured through burial, trenching, covering by rock dumping or tension stabilization by intermittent interventions. Consequences of failed on-bottom stability design has been experienced in the Gulf of Mexico due to the hurricanes Katrina, Rita and Ivan, which caused several instances of pipeline failures, severe lateral displacements of pipelines in the order of hundred meters, collisions with subsea installations, and major loss of production [1]. To minimize costs and environmental impact from burial or seabed interventions, it is highly attractive to optimize the on-bottom stability design such that a minimum of added weight or intervention is needed. On the other hand, examples from the Gulf of Mexico highlight that maintaining safety in operations is essential. Thus, any development or change to the industry practice must be based on research and sound empirical knowledge. The current design practice relies on simplified 1D and 2D computer tools [2,3] which are incapable of accounting correctly for effects such as development of axial friction and associated change of tension, the presence of free spans and curved sections along the route. The DROPS JIP initiated in 2017 by SINTEF Ocean aims to solve these issues and enhance the current design practice by developing robust and effective computational methods for 3D nonlinear time domain analysis.

* Corresponding author.
E-mail address: vegard.longva@sintef.no (V. Longva).

https://doi.org/10.1016/j.marstruc.2021.102985
Received 18 October 2020; Received in revised form 17 February 2021; Accepted 27 February 2021
Available online 10 April 2021

Nomenclature

D	Pipe external diameter $[L]$
E	Plastic energy related to soil penetration development $[F]$
f_F	Ratio between pipe–soil normal force and pipe submerged weight for sand yield force calculation, see Eq. (40) $[-]$
f_z	Ratio between pipe–soil normal force and pipe submerged weight for sand and clay penetration calculation, see Eq. (20) $[-]$
f	Yield function for passive pipe–soil force $[FL^{-1}]$
f_μ	Yield function for friction force $[FL^{-1}]$
F_p	Passive pipe–soil force in lateral direction $[FL^{-1}]$
F_p^{tr}	Elastic trial passive pipe–soil force in update algorithm $[FL^{-1}]$
$F_{p,\mu}^{tr}$	Elastic trial friction force in update algorithm $[FL^{-1}]$
F_μ	Friction pipe–soil force in lateral direction $[FL^{-1}]$
F_Y	Yield force $[FL^{-1}]$
F_Y^+	Yield force curve for $F_p > 0$ $[FL^{-1}]$
F_Y^-	Yield force curve for $F_p < 0$ $[FL^{-1}]$
F_{Y1}	Yield force at plastic displacement coordinate v_1 $[FL^{-1}]$
F_{Y2}	Yield force at breakout $[FL^{-1}]$
F_{Y3}	Residual yield force $[FL^{-1}]$
F_y	Total pipe–soil force in lateral direction $[FL^{-1}]$
F_z	Soil force in seabed normal direction $[FL^{-1}]$
$\overline{F}_z$	Normalized pipe–soil normal force, $\overline{F}_z = \frac{F_z}{S_u D}[-]$
G	Normalized undrained shear strength, $G = \frac{S_u}{\gamma_d D}[-]$
H_z	Plastic modulus due to penetration increase for passive pipe–soil force $[FL^{-2}]$
H_{v_p}	Plastic modulus due to pure plastic displacement change for passive pipe–soil force $[FL^{-2}]$
k	Elastic soil stiffness $[FL^{-2}]$
s_g	Pipe specific weight, $s_g = \frac{w}{w - w_s}[-]$
s_u	Undrained shear strength $[FL^{-2}]$
$s_{u_{z3}}$	Undrained shear strength value for activating residual penetration reduction due to stiff clay behavior $[FL^{-2}]$
t	Time $[T]$
v	Lateral pipe displacement $[L]$
v_e	Elastic lateral pipe displacement for passive pipe–soil force $[L]$
v_p	Plastic lateral pipe displacement for passive pipe–soil force $[L]$
$\dot{v}_p$	Rate of plastic lateral pipe displacement for passive pipe–soil force $[L/T]$
$\dot{v}_{p,\mu}$	Rate of plastic lateral pipe displacement for friction force $[L/T]$
v_{pa}	Amplitude of plastic lateral pipe displacement for passive pipe–soil force $[L]$
$\bar{v}_{pa}$	Applied amplitude of plastic lateral pipe displacement for clay passive pipe–soil force $[L]$
v_{pi}	Coordinates for plastic displacement used for defining yield force curve for passive pipe–soil force, $i = 1, 2, \ldots, 5$ $[L]$
w	Pipe weight in air $[FL^{-1}]$
w_s	Submerged pipe weight $[FL^{-1}]$
$\overline{w}_s$	Normalized pipe effective weight for clay, $\overline{w}_s = \frac{w_s f_z}{s_u D}[-]$
z	Penetration of pipe into the soil $[L]$
z_3	Penetration of pipe into the soil for calculation of residual passive pipe–soil yield force $[L]$
$\hat{z}_3$	Theoretical residual penetration of pipe into the soil $[L]$
z_e	Elastic penetration of pipe into the soil that is energy-conjugate with F_z $[L]$
z_p	Penetration of pipe into the soil induced by plastic lateral displacement v_p $[L]$
z_{max}	Maximum penetration of pipe into the soil. Reset if soil contact is lost. $[L]$
z_{lim}	Limit for stop of energy accumulation and soil penetration development $[L]$
κ_w	Non-dimensional proportionality factor for pipe buoyancy. Used for defining v_{pi}-coordinates for clay yield force curve, $\kappa_w = \frac{\gamma_w D^2}{w_s}$ $[-]$

κ_F	Non-dimensional pipe–soil normal force parameter for sand yield force calculation, $\kappa_F = \frac{\gamma_s D^2}{w_s f_F}$ [−]
κ_z	Non-dimensional pipe–soil normal force parameter for sand penetration computation, $\kappa_z = \frac{\gamma_s D^2}{w_s f_z}$ [−]
γ_d	Dry unit weight of soil $[FL^{-3}]$
γ_s	Submerged unit weight of soil $[FL^{-3}]$
γ_w	Unit weight of water $[FL^{-3}]$
$\dot{\lambda}$	Plastic rate parameter for passive pipe–soil force $[L]$
$\dot{\lambda}_\mu$	Plastic rate parameter for friction force $[L]$
μ	Friction coefficient in pipe lateral direction [−]
ξ	Percentage, $0 < \xi \leq 1$, of pipe diameter for defining number of displacement subincrements in force update scheme [−]
ΔE	Change of energy related to soil penetration development due to v_p, measured between previous equilibrium state and current configuration $[F]$
$\Delta\lambda$	Increment of plastic rate parameter for passive pipe–soil force in return map algorithm, measured between previous equilibrium state and current configuration $[L]$
Δv	Increment of displacement for passive pipe–soil force, measured between previous equilibrium state and current configuration $[L]$
$\delta\lambda$	Iterative increment of plastic rate parameter for passive pipe–soil force in return map algorithm $[L]$
δv	Subincrement of displacement for passive pipe–soil force in force update algorithm $[L]$

The current industry design practice for offshore pipelines is based on stepwise approaches, where aspects such as on-bottom stability, free-span design and global buckling are addressed separately. This is also reflected in design standards such as DNV-RP-F105 [4], DNV-RP-F109 [5] and DNV-RP-F110 [6], as well as the stand-alone software tools used for assessing the design such as the PONDUS program [3] for dynamic on-bottom stability analysis. The PONDUS hydrodynamic load model was developed based on model testing in the 1980s [7]. No consideration is made related to shallow water pipelines on cohesionless soils, 3D seabed erosion processes which may cause free spans and the validity of the hydrodynamic load models at free spans. Particularly, at free spans the lift, drag and inertia forces are generally reduced implying that the no gap assumption applied in the model tests is likely to be highly conservative. On the other hand, cross-flow vortex induced vibrations [8] in free spans may cause drag amplification in extreme environmental events, complicating the influence of free spans on lateral stability predictions. In the case of seabed erosion [9], design guidelines such as the DNV-RP-F109 code does not offer any detailed guidance on how to predict scour-induced changes to pipeline embedment and the effect of these changes on pipeline stability [10]. Ultimately, all of these shortcomings can be addressed by an integrated 3D analysis tool that can account for all relevant effects simultaneously in time domain. This would be beneficial for removing any unnecessary conservatism in current design practice. As a first step, the present work contributes by formulating a robust and effective pipe–soil algorithm for use in long-duration 3D nonlinear time domain analysis.

In the 1980s it was realized that the on-bottom stability design practice underpredicted the hydrodynamic loading from combined irregular waves and current. This motivated several research projects in which pipe–soil interaction was addressed by three major investigations, the PIPESTAB project [11], the AGA project [12,13] and a project at the Danish Hydraulic Institute [14]. The projects involved model testing of pipe–soil interaction for loose fine sand, loose medium coarse sand, dense medium coarse sand, soft clay and stiff clay. Soil resistance models were developed in the PIPESTAB project [15] and by using an energy-based method in the AGA project [16]. The PIPESTAB model was later revealed to be overly conservative by Verley and Reed [17], while the AGA implementation was found to exhibit non-physical behavior when used for certain realistic parameter ranges [18]. These shortcomings motivated further theoretical work which utilized dimensional analysis for fitting physically representative empirical equations to a large amount of data from the PIPESTAB, AGA and DHI laboratory tests. The efforts resulted in the development of the Verley and Sotberg model for sand [19,20] and the Verley and Lund model for clay [21]. These energy-based pipe–soil models form the basis for the dynamic on-bottom stability analysis recommended by the DNV-RP-F109 code, even though seabed erosion is not accounted for. Both pipe–soil interaction models were implemented in the PONDUS software [3]. The recent PILS JIP by DNV GL re-implemented the PONDUS clay and sand pipe–soil models in a 1D software tool [2]. The same pipe–soil interaction models were implemented in the AGA software in a recent work [22]. Hence, the PONDUS pipe–soil models for clay and sand are still regarded to represent state of the art for dynamic on-bottom stability analysis.

2. Formulation of elasto-plastic pipe–soil interaction models for sand and clay

2.1. General

On-bottom stability analysis typically involves simulation of several 3-hour irregular sea states with parameter variation of pipeline properties, soil properties and hydrodynamic properties. As stated by Griffiths et al. [23], 1D and 2D computer tools

are favored in current design practice due to computational efficiency, however, use of simplified tools imply a larger range of uncertainty for the predictions. This drawback may be avoided by using 3D analysis tools at the cost of increased computational efforts. The present work thus aims to extend the current design practice by developing a pipe–soil force update algorithm that fulfills the functional requirements of 3D nonlinear time domain analysis. This means that an efficient algorithm is required to avoid excessive CPU times. Robustness is equally important to avoid time-consuming modeling tweaks and analysis restarts. The main objective of our work has therefore been to develop robust and effective formulations of the pipe–soil interaction models proposed by Verley and Lund for clay and by Verley and Sotberg for sand. The work contributes thus with a revitalization of the pipe–soil models for use in modern 3D computer tools. Further, the governing equations of the pipe–soil interaction models are presented at a level of detail which so far has not been available in the public domain.

The clay and sand pipe–soil models are implemented in the PONDUS software [3] which is a 2D analysis tool based on the finite element method. This software is widely used in the industry for on-bottom stability analysis of pipelines, flexibles, power cables and umbilicals. The implementation is known to be very sensitive to the time step size, and may in some cases not converge to the correct solution even when the time step size is reduced. The initial implementation can be traced back to 1985 [24,25] and the elasto-plastic pipe–soil algorithm is today regarded as outdated. In modern finite element software, the backward-Euler update algorithm with consistent tangent stiffness proposed by Simo and Taylor [26] is recommended for elasto-plastic models. The idea of reusing the PONDUS algorithm was therefore rejected. Instead, the efforts were focused on identifying the weak points of PONDUS, and thereafter on developing a tailor-made pipe–soil algorithm that is effective and robust for nonlinear time domain analysis.

From a review of the PONDUS code, the following items were identified as plausible reasons for the poor numerical performance:

(1) The fully implicit backward-Euler method is not applied for time integration of the elasto-plastic material models, and hence instability may occur for large time steps.
(2) The passive pipe–soil force is assigned approximate elastic and plastic displacement components based on the Coulomb friction force.
(3) The yield criterion is not fulfilled exactly and thereby drift-off from the correct solution will occur for large time steps.
(4) An approximate tangent stiffness is applied which results in unnecessary global Newton–Raphson iterations.
(5) The hardening contribution from soil penetration is neglected. This results in unnecessary Newton–Raphson iterations for the global solution procedure and also for the local update scheme if based on implicit integration.
(6) The friction force algorithm is velocity-based which is known to exhibit poor numerical performance at reversal points due to the abrupt force change.
(7) The pipe–soil algorithm must distinguish between 7 states in terms of pipe–soil force and velocity direction.

More information about items 2, 6 and 7 is available in documentation from the PILS JIP [27].

In this work, the framework of computational plasticity is utilized to formulate the elasto-plastic pipe–soil interaction models. The time integration of the elasto-plastic models will therefore be based on the backward-Euler method, as opposed to item (1) above. Regarding items (2) and (3), the yield criterion will be handled consistently according to the backward-Euler integration scheme and the true elastic and the plastic displacement components will be applied. Consequently, and opposed to item (4) above, the update scheme can be linearized to obtain the tangent stiffness for the global Newton–Raphson solution procedure. A further improvement of the convergence properties is achieved by accounting for hardening due to soil penetration, Ref. item (5). In view of item (6), the friction force will be based on a displacement-based penalty regularization to avoid the issue of abrupt force changes. Rather than to distinguish between several material states as in item (7), the updating will be performed by a predictor–corrector algorithm based on the concept of elastic trial force.

The total lateral pipe–soil force F_y consists of two contributions,

$$F_y = F_\mu + F_p \tag{1}$$

where F_μ is a pure friction force and F_p is the passive pipe–soil force. Both force components are assigned independent models in this work, which is in contrast to item (2) above where the displacement components of the friction force are employed for updating the passive pipe–soil force.

Sections 2.2 and 2.3 define the pipe–soil normal contact force and the soil penetration. The constitutive model formulated for F_p is presented in Sections 2.4–2.6. The optimization techniques for the force update algorithm for F_p are elaborated in 2.7 and 2.8. The constitutive model for F_μ is presented in Section 2.9. Section 3 contains a verification study focusing on the numerical performance and enhancements achieved compared to the PONDUS software. The conclusions of the work are summarized in Section 4.

2.2. Hyper-elastic model for normal direction

2.2.1. Sand

The pipe–soil distributed contact force F_z in the seabed normal direction is assigned the following hyper-elastic relation for sand [3],

$$F_z = \gamma_s D^2 \left(\frac{z_e}{0.037 D} \right)^{1.5} \tag{2}$$

where z_e is the elastic soil penetration defined in Fig. 1 which is energy-conjugate to F_z. The soil submerged unit weight is denoted γ_s and D is the pipe external diameter.

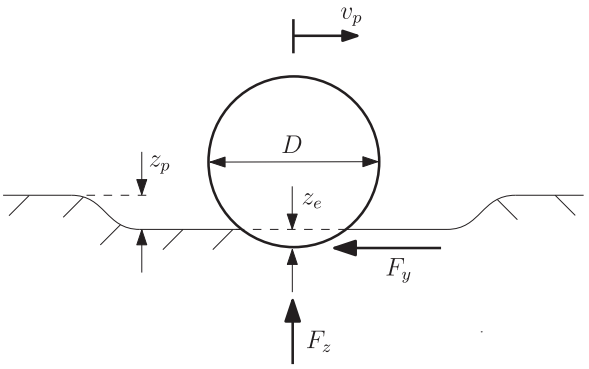

Fig. 1. Definition of soil penetration, lateral plastic displacement v_p and pipe–soil forces F_y and F_z.

2.2.2. Clay

The hyper-elastic relation between the distributed normal contact force F_z and the elastic soil penetration z_e for clay is given by [3],

$$z_e = 0.0071D\left(\frac{G^{0.3}}{s_u D}F_z\right)^{3.2} + 0.062D\left(\frac{G^{0.3}}{s_u D}F_z\right)^{0.7} \tag{3}$$

where the undrained shear strength is denoted s_u and G is defined in Eq. (18). A local Newton–Raphson scheme is applied for solving Eq. (3) with respect to F_z.

2.3. Soil penetration

The soil penetration consists of two components as shown in Fig. 1,

$$z = z_p(v_p) + z_e(F_z) \tag{4}$$

where z_p is the soil penetration induced by the pipeline lateral plastic displacement v_p. For small cyclic lateral displacements, the penetration z_p increases due to berm formation and thereby increases the passive pipe–soil force F_p in Eq. (1), whereas for larger displacements the pipeline will break out of the berm and F_p decreases to a residual value. The pipeline lateral displacement is thus dependent on the penetration z_p, which itself is dependent on the lateral displacement. The penetration development models for clay and sand are presented in Sections 2.5.3 and 2.6.4, respectively. It is emphasized that the elastic soil penetration z_e is independent of z_p.

2.4. Elasto-plastic model for passive pipe–soil force

The pipe–soil interaction models are analogous to elasto-plastic material models used in plasticity theory. Standard elasto-plastic stress update schemes can therefore be applied for time integration of the pipe–soil models. The starting point is to describe the pipe–soil models by variables that are analogous to stress and strain, as well as defining a hardening rule, a flow rule and a yield criterion.

An additive decomposition of the lateral pipe displacement v is applied,

$$v = v_e + v_p \tag{5}$$

where v_e and v_p denote the elastic and plastic components, respectively. The lateral passive pipe–soil force F_p is computed by the following elastic relation,

$$F_p = kv_e \tag{6}$$

where k is the elastic lateral stiffness of the soil.

The yield criterion is expressed in terms of the yield force F_Y as follows,

$$f\left(F_p, v_p, F_z\right) = \left[F_p - F_Y\left(v_p, z(v_p, F_z)\right)\right]\operatorname{sign}\left(F_p\right) \tag{7}$$

where z is the soil penetration defined in Eq. (4). The yield criterion in Eq. (7) must obey the constraint $f \leq 0$,

$$f = 0 \quad \rightarrow \quad \text{plastic domain} \tag{8}$$

$$f < 0 \quad \rightarrow \quad \text{elastic domain} \tag{9}$$

$$f > 0 \quad \rightarrow \quad \text{inadmissible} \tag{10}$$

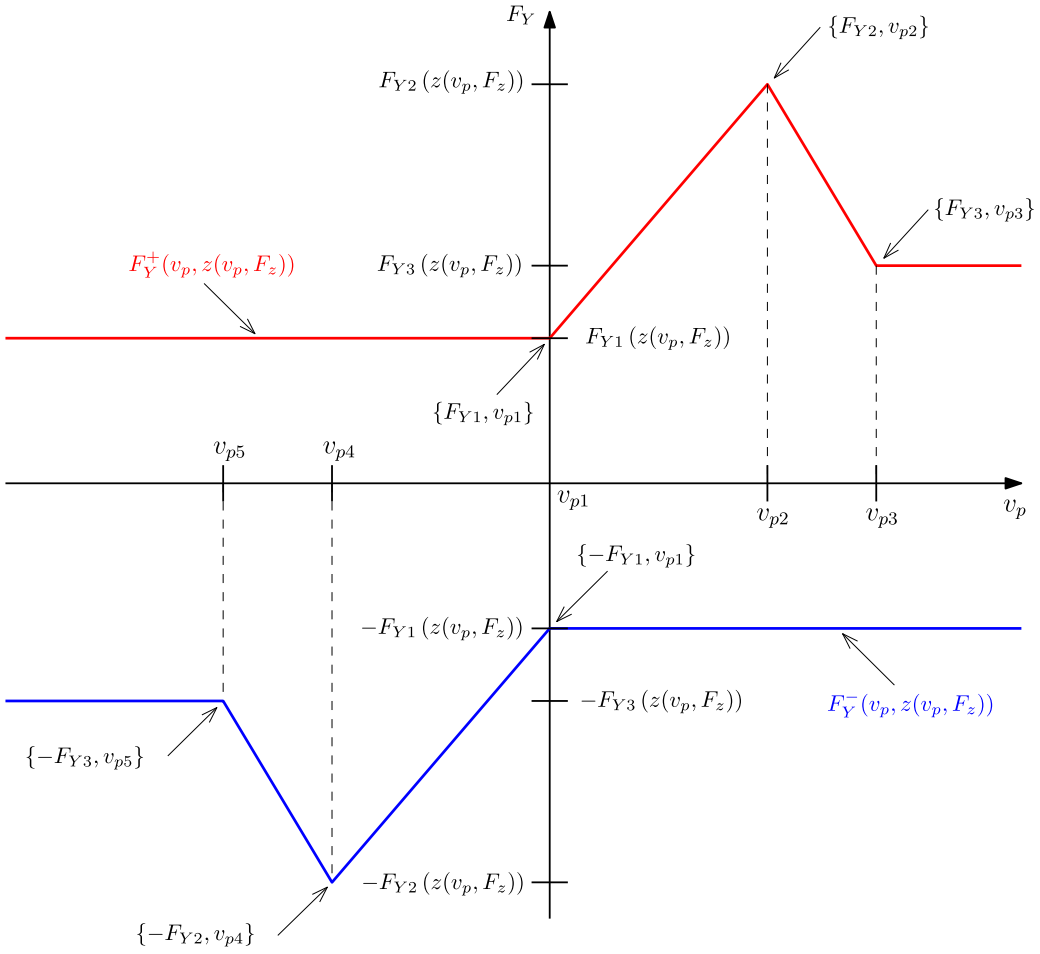

Fig. 2. Initial yield force as a function of plastic displacement.

The yield force function F_Y is shown graphically in Fig. 2 and can be expressed as follows,

$$F_Y\left(v_p, z(v_p, F_z)\right) = \begin{cases} F_Y^+\left(v_p, z(v_p, F_z)\right) & \text{if} \quad F_p > 0 \\ F_Y^-\left(v_p, z(v_p, F_z)\right) & \text{if} \quad F_p < 0 \end{cases} \tag{11}$$

The yield force curves F_Y^+ and F_Y^- in Fig. 2 appears to be a piecewise linear function of v_p, however, the points on the vertical axis are a function of the soil penetration which in turn depends on v_p, i.e. $F_{Yi}\left(z(v_p, F_z)\right)$. Hence, the response path of the passive pipe–soil force F_p is nonlinear in terms of v_p as illustrated in Fig. 3.

The evolution of the plastic displacement is assumed to follow a non-associative flow rule,

$$\dot{v}_p = \dot{\lambda}\frac{\partial f}{\partial F_p} = \dot{\lambda}\,\mathrm{sign}(F_p) \tag{12}$$

where $\dot{\lambda}$ is the plastic rate parameter. Both here and in the sequel the superposed dot means time derivative. It can be proven that the constraint $\dot{\lambda} \geq 0$ must be fulfilled, where $\dot{\lambda} = 0$ in the elastic domain, $\dot{\lambda} > 0$ in the plastic domain and $\dot{\lambda} < 0$ is inadmissible.

The hardening rule is expressed by the sum,

$$\dot{F}_Y = \dot{\lambda}H_{v_p} + \dot{\lambda}H_z \tag{13}$$

where the plastic modulus associated with pure plastic displacement is given by,

$$H_{v_p} = \frac{\partial F_Y}{\partial v_p} \tag{14}$$

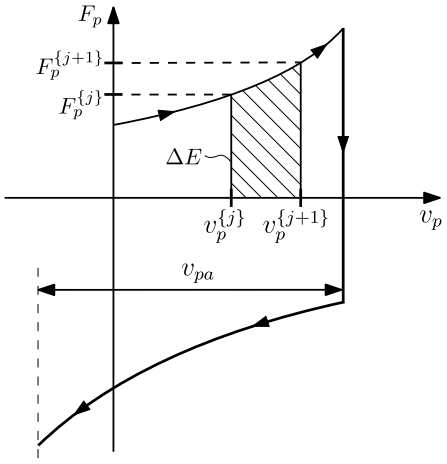

Fig. 3. Definition of plastic displacement amplitude v_{pa} and energy increment ΔE.

and the plastic modulus due to increase of soil penetration z is expressed as,

$$H_z = \begin{cases} \frac{\partial F_y}{\partial z}\frac{\partial z}{\partial E}\frac{\partial E}{\partial v_p} & \text{if} \quad \dot{z}_p > 0 \\ 0 & \text{if} \quad \dot{z}_p \le 0 \end{cases} \tag{15}$$

where E is the energy defined in Sections 2.5.3 and 2.6.4. In addition to Eq. (13), the yield force may also change because of horizontal translation of the curve shown in Fig. 2. The translation is expressed in terms of the following rules for the horizontal coordinates,

$$\dot{v}_{pi} = \dot{\lambda} \quad \text{if} \quad v_p \ge v_{p2} \quad F_p > 0 \quad , \quad i = 1, 2, \dots, 5 \tag{16}$$

$$\dot{v}_{pi} = -\dot{\lambda} \quad \text{if} \quad v_p \le v_{p4} \quad F_p < 0 \quad , \quad i = 1, 2, \dots, 5 \tag{17}$$

For the sand model, there is an additional translation of the points v_{p2} and v_{p4} during initial plastic loading as described in Section 2.6.3. The initial values of the coordinates v_{pi} and F_{Yi} are presented in Sections 2.5.2 and 2.6.2.

In line with the PONDUS code and Lieng et al. [28], the yield force is assumed to be symmetric with respect to negative and positive pipe–soil forces, meaning that hardening and translation of the horizontal coordinates for a positive loading also affects the negative force curve and vice versa. In other words, the soil resistance is equal in both directions, and is increased or reduced simultaneously on both sides of the pipe. This symmetry could be utilized in order to simplify the governing equations. However, in view of possible future model enhancements, the general form presented above with negative and positive yield force curves was chosen.

It is emphasized that the elasto-plastic model is rate-independent. The plastic rate parameter $\dot{\lambda}$ is merely a proportionality factor that can be eliminated in the implementation, meaning that the lateral passive pipe–soil force is independent of the velocity.

The clay and sand models apply a similar format for the governing equations, however, they differ in terms of the parametrizations used for the yield force curve and the soil penetration development. The expressions assigned to the yield force F_Y in Eq. (7) and the computation of soil penetration are elaborated in Sections 2.5 and 2.6.

2.5. Clay passive pipe–soil force

2.5.1. Governing parameters

The governing parameters for the clay model is the dry unit weight of the soil γ_d, the undrained shear strength of the soil s_u, the instantaneous seabed normal contact force F_z, the pipe submerged weight w_s, the pipe external diameter D and the unit weight of water γ_w. These quantities are involved in the following non-dimensional parameters,

$$G = \frac{s_u}{\gamma_d D} \tag{18}$$

$$\overline{F}_z = \begin{cases} 0.05 & \text{if} \quad \frac{F_z}{s_u D} < 0.05 \\ \frac{F_z}{s_u D} & \text{if} \quad \frac{F_z}{s_u D} > 0.05 \end{cases} \tag{19}$$

$$\overline{w}_s = \frac{w_s}{s_u D} f_z \qquad f_z = \begin{cases} 0.01 & \text{if} \quad \frac{F_z}{w_s} < 0.01 \\ \frac{F_z}{w_s} & \text{if} \quad \frac{F_z}{w_s} > 0.01 \end{cases} \tag{20}$$

$$\kappa_w = \begin{cases} \frac{\gamma_w D^2}{w_s} & \text{if} \quad 3.0 < \frac{\gamma_w D^2}{w_s} < 25.0 \\ 25.0 & \text{if} \quad \frac{\gamma_w D^2}{w_s} > 25.0 \\ 3.0 & \text{if} \quad \frac{\gamma_w D^2}{w_s} < 3.0 \end{cases} \tag{21}$$

where G is the normalized undrained shear strength, $\overline{F}_z$ is the normalized seabed contact force in the normal direction, $\overline{w}_s$ is the normalized effective pipe weight and κ_w is the normalized pipe buoyancy proportionality factor.

2.5.2. Yield force curve

The initial plastic displacement coordinates in Fig. 2 are defined by,

$$v_{p1} = 0.0 \tag{22}$$

$$v_{p2} = 0.75D \tag{23}$$

$$v_{p3} = 0.6D\left(\frac{5.5}{\kappa_w} + 1\right) + v_{p2} \tag{24}$$

$$v_{p4} = -v_{p2} \tag{25}$$

$$v_{p5} = -v_{p3} \tag{26}$$

and the yield force coordinates in Fig. 2 are calculated as,

$$F_{Y1} = F_{Y3} \tag{27}$$

$$F_{Y2} = 4.13 s_u D\left(\frac{z}{D}\right)^{1.31} G^{-0.392} \tag{28}$$

$$F_{Y3} = 4.13 s_u D\left(\frac{z_3}{D}\right)^{1.31} G^{-0.392} \tag{29}$$

where z is the soil penetration defined by Eq. (4) and the residual penetration z_3 is given by,

$$\begin{aligned} z_3 &= \hat{z}_3\left(\frac{s_{u_{z3}}}{s_u}\right)^4 \quad \text{if} \quad s_u > s_{u_{z3}} \\ z_3 &= \hat{z}_3 \quad \text{if} \quad s_u \le s_{u_{z3}} \end{aligned} \tag{30}$$

where $s_{u_{z3}}$ is the undrained shear strength value for activating residual penetration reduction due to stiff clay behavior. The PONDUS code applies $s_{u_{z3}} = 4\,\text{kPa}$. The quantity $\hat{z}_3$ is the soft clay residual penetration calculated as,

$$\hat{z}_3 = 0.0071 D\left(\overline{w}_s G^{0.3}\right)^{3.2} + 0.062 D\left(\overline{w}_s G^{0.3}\right)^{0.7} \tag{31}$$

which coincide with the elastic penetration of a pipe node with contact force equal to the pipeline submerged weight w_s, see Eq. (3).

2.5.3. Soil penetration and energy

The soil penetration z depends on the energy E as follows,

$$z = 0.12 D\left(\frac{E}{s_u D^2}\right)^{0.32} (\overline{w}_s)^{0.637}\left(\frac{\tilde{v}_{pa}}{D}\right)^{-0.25} \tag{32}$$

in which $\tilde{v}_{pa}$ represents the plastic displacement amplitude measured from the last zero-crossing of F_p according to,

$$\tilde{v}_{pa} = \begin{cases} 0.05D & \text{if} \quad \frac{v_{pa}}{D} < 0.05 \\ v_{pa} & \text{if} \quad \frac{v_{pa}}{D} > 0.05 \end{cases} \tag{33}$$

where v_{pa} is illustrated in Fig. 3,

Increase of energy ΔE giving increase of z_p is computed by trapezoidal integration during the pre-breakout phase. Energy is accumulated only in the first half of the pre-breakout range according to,

$$\Delta E = \frac{F_p + F_p^{\{i-1\}}}{2}\left(v_p - v_p^{\{i-1\}}\right) \quad \text{if} \quad v_p < \frac{v_{p1} + v_{p2}}{2} \quad F_p, F_p^{\{i-1\}} > 0 \quad z < z_{lim} \tag{34}$$

$$\Delta E = \frac{F_p + F_p^{\{i-1\}}}{2}\left(v_p - v_p^{\{i-1\}}\right) \quad \text{if} \quad v_p > \frac{v_{p1} + v_{p4}}{2} \quad F_p, F_p^{\{i-1\}} < 0 \quad z < z_{lim} \tag{35}$$

where the energy increment ΔE is illustrated in Fig. 3. Superscript $\{i-1\}$ is introduced for quantities referring to the previous equilibrium configuration. Both here and in the sequel, F_p and v_p refer to the current configuration after F_p has been mapped onto the yield surface $f = 0$ by applying the return map algorithm in Section 2.7.2. Energy is not accumulated if the soil penetration in Eq. (32) exceeds the limit,

$$z_{lim} = \min\left\{ 0.5D \;,\; 1.1 D \overline{w}_s G^{0.54}\left\{\frac{\tilde{v}_{pa}}{D}\right\}^{-0.25} \right\} \tag{36}$$

The energy remains constant on the intervals $0.5\left(v_{p1}+v_{p2}\right) \leq v_p \leq v_{p2}$ and $v_{p4} \leq v_p \leq 0.5\left(v_{p1}+v_{p4}\right)$, and reduces during pipe breakout. Due to Eqs. (16) and (17), the force F_p computed by the return map in Section 2.7.2 is equal to F_{Y2} and thus the soil penetration can be calculated by Eq. (28) during post-breakout according to,

$$\begin{aligned} z &= D\left(\frac{\left|F_p\right|}{4.13 s_u D G^{-0.392}}\right)^{\frac{1}{1.31}} \geq z_3 \\ \text{if} \quad & v_p \geq v_{p2} \quad F_p, F_p^{\{i-1\}} > 0 \\ \text{or if} \quad & v_p \leq v_{p4} \quad F_p, F_p^{\{i-1\}} < 0 \end{aligned} \tag{37}$$

which corresponds to the following reduced energy,

$$E = s_u D^2 \left(\frac{z}{0.12 D \left(\overline{w}_s\right)^{0.637} \left(\frac{\tilde{v}_{pa}}{D}\right)^{-0.25}}\right)^{\frac{1}{0.32}} \tag{38}$$

2.5.4. Validity range

The clay model is valid for the following parameter ranges,

$$\begin{aligned} s_u &= [\,0.8\,\text{kPa}, 70\,\text{kPa}\,] \\ G &= [\,0.02, 5.0\,] \\ D &= [\,0.15\,\text{m}, 1.0\,\text{m}\,] \\ \frac{z}{D} &= [\,0.0, 0.35\,] \\ \frac{v_{pa}}{D} &= [\,0.05, 1.0\,] \\ \overline{F}_z &= [\,0.05, 7.5\,] \\ \kappa_w &= [\,3.0, 25.0\,] \\ s_g &= [\,1.06, 2.5\,] \end{aligned}$$

where s_g is the pipe specific weight defined as the ratio between the pipe weight in air and the buoyancy of the pipe,

$$s_g = \frac{w}{w - w_s} \tag{39}$$

2.6. Sand passive pipe–soil force

2.6.1. Governing parameters

The governing parameters for the sand model is the pipe submerged weight w_s, the instantaneous seabed normal contact force F_z, the submerged unit weight of soil γ_s and the pipe diameter D. The following non-dimensional parameters are involved in the governing equations,

$$f_F = \begin{cases} 0.2 & \text{if} \quad \frac{F_z}{w_s} < 0.2 \\ \frac{F_z}{w_s} & \text{if} \quad \frac{F_z}{w_s} > 0.2 \end{cases} \tag{40}$$

$$\kappa_z = \begin{cases} 3.0 & \text{if} \quad \frac{\gamma_s D^2}{w_s f_z} < 3.0 \\ \frac{\gamma_s D^2}{w_s f_z} & \text{if} \quad \frac{\gamma_s D^2}{w_s f_z} > 3.0 \end{cases} \tag{41}$$

$$\kappa_F = \begin{cases} 20.0 & \text{if} \quad \frac{\gamma_s D^2}{w_s f_F} > 20.0 \\ \frac{\gamma_s D^2}{w_s f_F} & \text{if} \quad \frac{\gamma_s D^2}{w_s f_F} < 20.0 \end{cases} \tag{42}$$

where f_F is the ratio between the seabed normal contact force and the pipe submerged weight, applied for computation of the yield force curve. The parameter κ_z defines the maximum allowable soil penetration and κ_F is involved in the yield force expressions.

2.6.2. Yield force curve

The initial plastic displacement coordinates in Fig. 2 are defined by,

$$v_{p1} = 0.0 \tag{43}$$

$$v_{p2} = 0.1 D \tag{44}$$

$$v_{p3} = \begin{cases} 0.6D + v_{p2} & \text{if} \quad z_{max} \geq 0.15D \\ 0.1D + 3.3z_{max} + v_{p2} & \text{if} \quad z_{max} < 0.15D \end{cases} \tag{45}$$

$$v_{p4} = -v_{p2} \tag{46}$$

$$v_{p5} = -v_{p3} \tag{47}$$

where z_{max} is the maximum soil penetration during the simulation, which is reset if seabed contact is lost. The yield force coordinates in Fig. 2 are calculated as,

$$F_{Y1} = 0.3F_{Y2} \tag{48}$$

$$F_{Y2} = \gamma_s D^2 \left(5 - 0.15\kappa_F\right) \left(\frac{z}{D}\right)^{\frac{5}{4}} \tag{49}$$

$$F_{Y3} = \gamma_s D^2 \left(5 - 0.15\kappa_F\right) \left(\frac{z_3}{D}\right)^{\frac{5}{4}} \tag{50}$$

where z is the soil penetration and the residual penetration z_3 is given by,

$$z_3 = \left(0.82 - 3.2\left(\frac{z_{max}}{D}\right)\right) z_{max} \tag{51}$$

2.6.3. Initial translation rule for v_{p2} and v_{p4}

The points v_{p2} and v_{p4} in Fig. 2 are translated horizontally prior to pipe breakout according to,

$$\dot{v}_{p2} = \dot{\lambda} \quad \dot{v}_{p4} = -\dot{\lambda} \quad \text{if} \quad v_p \geq v_{p2} \quad \left(v_{p2} - v_{p1}\right) < 0.7D \quad F_p > 0 \quad , \quad i = 2,4 \tag{52}$$

$$\text{or if} \quad v_p \leq v_{p4} \quad \left(v_{p1} - v_{p4}\right) < 0.7D \quad F_p < 0 \quad , \quad i = 2,4 \tag{53}$$

The translation above is applied until v_{p1} and v_{p2} are separated by $0.7D$, and likewise for v_{p1} and v_{p4}. Thereafter, the translation rules in Eqs. (16) and (17) apply.

2.6.4. Soil penetration and energy

The soil penetration z is linked to the energy E as follows,

$$z = 0.23D \left(\frac{E w_s f_z}{\gamma_s^2 \left(\frac{\tilde{v}_{pa}}{D}\right)^{0.5} D^5} \right)^{0.32} \tag{54}$$

where f_z is defined identically as in Eq. (20) for the clay model, and $\tilde{v}_{pa}$ represents the plastic displacement amplitude measured from the last zero-crossing of F_p according to,

$$\tilde{v}_{pa} = \begin{cases} 0.1D & \text{if} \quad \frac{v_{pa}}{D} < 0.1 \\ v_{pa} & \text{if} \quad \frac{v_{pa}}{D} > 0.1 \end{cases} \tag{55}$$

where v_{pa} is illustrated in Fig. 3.

Increase of energy ΔE giving increase of z_p is present during the whole pre-breakout phase and is computed by trapezoidal integration as follows,

$$\Delta E = \frac{F_p + F_p^{\{i-1\}}}{2} \left(v_p - v_p^{\{i-1\}}\right) \quad \text{if} \quad v_p < v_{p2} \quad F_p, F_p^{\{i-1\}} > 0 \tag{56}$$

$$\Delta E = \frac{F_p + F_p^{\{i-1\}}}{2} \left(v_p - v_p^{\{i-1\}}\right) \quad \text{if} \quad v_p > v_{p4} \quad F_p, F_p^{\{i-1\}} < 0 \tag{57}$$

where the energy increment ΔE is illustrated in Fig. 3. Superscript $\{i-1\}$ marks that the quantity refers to the previous equilibrium configuration. F_p and v_p refer to the current configuration after F_p has been mapped onto the yield surface $f = 0$. Energy is not accumulated and further soil penetration stops if z in Eq. (54) exceeds the limit,

$$z_{lim} = \sqrt{\frac{v_{pa}}{D\kappa_z}} \tag{58}$$

The energy and the soil penetration reduce during pipe breakout. As explained for the clay model in Section 2.5.3, the soil penetration can be computed based on the breakout force in Eq. (49),

$$\begin{aligned} z = & D \left(\frac{\left|F_p\right|}{\gamma_s D^2 \left(5 - 0.15\kappa_F\right)} \right)^{\frac{4}{5}} \geq z_3 \\ \text{if} \quad & v_p \geq v_{p2} \quad F_p, F_p^{\{i-1\}} > 0 \\ \text{or if} \quad & v_p \leq v_{p4} \quad F_p, F_p^{\{i-1\}} < 0 \end{aligned} \tag{59}$$

which corresponds to the following reduced energy,

$$E = \frac{\gamma_s^2 \left(\frac{\bar{v}_{pa}}{D}\right)^{0.5} D^5}{w_s f_z} \left(\frac{z}{0.23D}\right)^{\frac{1}{0.32}} \tag{60}$$

2.6.5. Validity range

The sand model is valid for the following parameter ranges,

$$D = [\,0.3\,\text{m}, 1.0\,\text{m}\,]$$
$$\frac{z}{D} = [\,0.0, 0.35\,]$$
$$\frac{v_{pa}}{D} = [\,0.1, 1.0\,]$$
$$\kappa_F \leq 20.0$$
$$\kappa_z \geq 3.0$$

2.7. Force update algorithm

A backward-Euler update scheme based on elastic predictor and plastic corrector is applied. The algorithm is fully implicit in order to allow for large incremental steps. Further, the update scheme can be linearized to obtain the tangent stiffness for the global Newton–Raphson solution procedure.

2.7.1. Trial step

The force update is displacement-driven,

$$v = v^{\{i-1\}} + \Delta v \tag{61}$$

meaning that the displacement increment Δv is a fixed quantity during the updating. All quantities that refer to the previous equilibrium state are denoted by superscript $\{i-1\}$, while no superscript means that the current configuration is the reference.

The trial step is also referred to as the elastic predictor part of the algorithm. This is because the concept of elastic trial force is applied, where the whole displacement increment is assumed to be elastic according to,

$$F_p^{tr} = F_p^{\{i-1\}} + k\Delta v \tag{62}$$

The elastic trial force F_p^{tr} is inserted into the yield criterion in Eq. (7) to check if the increment indeed is fully elastic,

$$f\left(F_p^{tr}, v_p^{\{i-1\}}, F_z\right) \geq 0 \quad \rightarrow \quad \text{plastic increment} \tag{63}$$
$$f\left(F_p^{tr}, v_p^{\{i-1\}}, F_z\right) < 0 \quad \rightarrow \quad \text{elastic increment} \tag{64}$$

If the increment is fully elastic, the force update algorithm will be terminated and the global Newton–Raphson tangent stiffness will be set equal to the elastic soil stiffness k. Otherwise, the return map algorithm in Section 2.7.2 must be applied.

2.7.2. Return map

The return map, which also is referred to as the plastic corrector, is activated if the increment is not fully elastic. The mapping of the elastic trial force onto the yield surface $f=0$ involves the following equations,

$$F_p = F_p^{tr} - k\Delta\lambda \tag{65}$$
$$f\left(F_p, v_p, F_z\right) = 0 \tag{66}$$

where the normal force F_z is computed by the global solution procedure and is thus a fixed quantity within the force update. Eqs. (65) and (66) are solved by the following Newton–Raphson iterative solution scheme,

$$\delta\lambda^{\{k\}} = \frac{f\left(F_p^{\{k\}}, v_p^{\{k\}}, F_z\right)}{k + H_{v_p}^{\{k\}} + H_z^{\{k\}}} \tag{67}$$
$$\Delta\lambda^{\{k+1\}} = \delta\lambda^{\{k\}} + \Delta\lambda^{\{k\}} \tag{68}$$
$$F_p^{\{k+1\}} = F_p^{\{k\}} + k\left(\Delta v - \Delta\lambda^{\{k+1\}}\right) \tag{69}$$
$$v_p^{\{k+1\}} = v_p^{\{k\}} + \delta\lambda^{\{k\}} \tag{70}$$

where superscript $\{k\}$ is the iteration index. The following initial values are applied for $k=0$,

$$\Delta\lambda^{\{0\}} = 0 \tag{71}$$
$$v_p^{\{0\}} = v_p^{\{i-1\}} \tag{72}$$

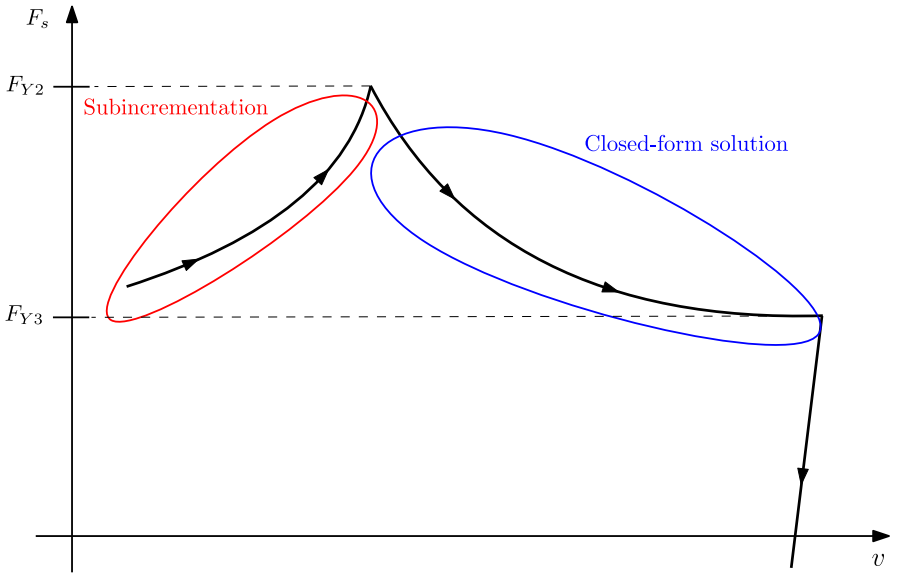

Fig. 4. Algorithm optimization techniques.

$$F_p^{\{0\}} = F_p^{tr} \tag{73}$$

where superscript $\{i-1\}$ refers to the previous equilibrium state.

2.7.3. Tangent stiffness

The tangent stiffness for the global Newton–Raphson solution procedure is obtained by linearizing the force update scheme. The linearization is performed after the force F_p has been returned to the yield surface $f=0$. After the force updating, the normal force F_z is not fixed anymore and should thus be accounted for in the linearization. However, that would lead to a one-way coupling between the lateral and normal directions resulting in a non-symmetric stiffness matrix. Hence, only the force F_p and the displacement v_p in the lateral direction are considered when the tangent stiffness is developed.

2.8. Algorithm optimization

The return map in Section 2.7.2 is based on backward-Euler integration and can thus handle large steps without introducing numerical instability. However, testing revealed that accuracy was actually the limiting factor for the time step size, particularly when the passive pipe–soil force undergoes large changes during energy accumulation in the pre-breakout phase and during the post-breakout phase where the passive pipe–soil force decays to F_{Y3}. As illustrated in Fig. 4, two optimization techniques were therefore developed to increase the limiting time step size.

2.8.1. Subincrementation for pre-breakout phase

The passive pipe–soil force undergoes a nonlinear increase with respect to the lateral displacement during the pre-breakout phase as shown in Fig. 4. The nonlinear response arise due to hardening introduced by the soil penetration increase, which is linked the lateral displacement through the increase of energy computed by Eqs. (34), (35), (56) and (57). The accuracy of the energy computation is therefore critical, in which small time steps generally is required to capture accurately the nonlinear increase of the yield force.

In this work, the use of small time steps in the pre-breakout phase is avoided by using subincrements within the return map. This means that the displacement increment is subdivided into m subincrements of equal magnitude,

$$\delta v = \frac{\Delta v}{m} \qquad m = \text{ceil}\left(\frac{\Delta v}{\xi D}\right) \qquad \xi = 0.025 \tag{74}$$

where the ceil-function maps the argument value to the least integer greater than or equal to the argument. The selected value of ξ was found by comparing numerous simulations with subincrementation against simulations with very fine time resolution. The subincrements are inserted into the force update algorithm in Section 2.7, which checks for yielding and if relevant maps the trial elastic force subincrement back to the yield surface $f=0$. Thereafter, the state variables are updated before the next subincrement is applied. The subincrementation technique is attractive compared to using smaller time steps, especially for large finite element models where the computational cost per time step is significant.

2.8.2. Closed-form solution for post-breakout phase

There is no hardening due to increase of soil penetration z_p in the post-breakout phase, i.e. $H_z = 0$ in Eq. (15), and the hardening from H_{v_p} in Eq. (14) would alone result in a linear reduction of the pipe–soil force. However, the yield force curve undergoes horizontal translation according to Eqs. (16) and (17). This implies that the force computed by the return map is equal to F_{Y2}. Based on this, the pipe–soil force will decrease in a nonlinear manner until the residual plateau at F_{Y3} is reached asymptotically for large displacements. Small time steps must generally be applied to capture the nonlinear decrease of the pipe–soil force with sufficient accuracy, especially in the vicinity of breakout where the slope is large.

In this work, the time step size limitation is avoided by describing the continuous nonlinear reduction of the yield force by the following differential equations,

$$\frac{\mathrm{d}F_Y}{\mathrm{d}v_p} = \frac{F_{Y3} - F_Y}{v_{p3} - v_{p2}} \qquad \text{if} \qquad v_p \geq v_{p2} \quad F_p > 0 \tag{75}$$

$$\frac{\mathrm{d}F_Y}{\mathrm{d}v_p} = \frac{F_{Y3} - F_Y}{v_{p4} - v_{p5}} \qquad \text{if} \qquad v_p \leq v_{p4} \quad F_p < 0 \tag{76}$$

which have solutions,

$$F_Y\left(v_p\right) = \quad F_{Y3} + \left(F_{Y2} - F_{Y3}\right) \cdot \exp\left\{-\frac{v_p - v_{p2}}{v_{p3} - v_{p2}}\right\} \qquad \text{if} \qquad v_p \geq v_{p2} \quad F_p > 0 \tag{77}$$

$$F_Y\left(v_p\right) = -F_{Y3} + \left(F_{Y3} - F_{Y2}\right) \cdot \exp\left\{-\frac{v_{p4} - v_p}{v_{p4} - v_{p5}}\right\} \qquad \text{if} \qquad v_p \leq v_{p4} \quad F_p < 0 \tag{78}$$

The closed-form solutions are applied in Eq. (67) during the return mapping by inserting Eqs. (77) and (78) into the yield criterion in Eq. (7) and into the definition of the hardening H_{v_p} in Eq. (14). F_{Y2} and F_{Y3} are updated at every global Newton–Raphson iteration to account for the change of elastic soil penetration z_e and normal direction contact force F_z. Note that the yield force according to Eqs. (77) and (78) approaches the residual yield force F_{Y3} asymptotically for large values of v_p.

The closed-form solution in Eqs. (77) and (78) captures the exact continuous change described by Eqs. (75) and (76) regardless of the time step size. A numerical solution would instead approximate the pipe–soil force change by a limited number of non-continuous slopes, $\Delta F_Y / \Delta v_p$, governed by the time step size. In other words, the closed-form solution removes the time step size limitation locally within the return map algorithm. This is in contrast to PONDUS where stepwise linear increments are used for describing the nonlinear reduction of the passive pipe–soil force. PONDUS is thus restricted to apply small time steps to capture the true nonlinear reduction of the passive pipe–soil force.

With the closed-form solution there is no need for special treatment of the case where the increment exceeds $\Delta v_p^{lim} = \left(v_{p3} - v_{p2}\right)$, which theoretically can occur if large time steps are applied for very unstable pipelines subjected to extreme lateral loading. This special case is described in the PILS documentation [27], where the passive pipe–soil force surprisingly is set equal to F_{Y1} instead of F_{Y3} when the increment exceeds Δv_p^{lim}, which is in line with the PONDUS code. With this approach, the pipe–soil force becomes dependent on the time step size, where small steps will capture the true force decay to F_{Y3} and a spurious abrupt force change to F_{Y1} will occur for very large steps. This issue is irrelevant when the yield force is calculated analytically according to Eqs. (77) and (78).

2.9. Elasto-plastic model for friction force

The friction model is based on the same ingredients and framework equations as presented in Section 2.4. Only differences compared to the passive pipe–soil force model will be elaborated here.

A standard Coulomb friction model is employed with yield criterion expressed by,

$$f_\mu\left(F_\mu, F_z\right) = \left[F_\mu - \mu F_z\right] \operatorname{sign}\left(F_\mu\right) \qquad F_z \geq 0 \tag{79}$$

where μ is the pipe–soil lateral friction coefficient and F_z is the pipe–soil force in the normal direction.

An associative flow rule would introduce separation forces in the normal direction due to the form of f_μ. Hence, the flow rule is selected to be non-associative according to,

$$\dot{v}_{p,\mu} = \dot{\lambda}_\mu \frac{\partial f_\mu}{\partial F_\mu} = \dot{\lambda}_\mu \tag{80}$$

The hardening is zero because F_z in Eq. (79) is calculated by the global solution procedure and thus kept fixed within the local update scheme. A beneficial consequence of zero hardening is that the iterative return map algorithm in Section 2.7.2 is avoided. Instead, the following closed-form solution is applied for mapping the elastic trial force onto the yield surface $f_\mu = 0$,

$$F_\mu = \mu F_z \operatorname{sign}\left(F_\mu^{tr}\right) \tag{81}$$

where F_μ^{tr} is the elastic trial force computed similarly as in Eq. (62).

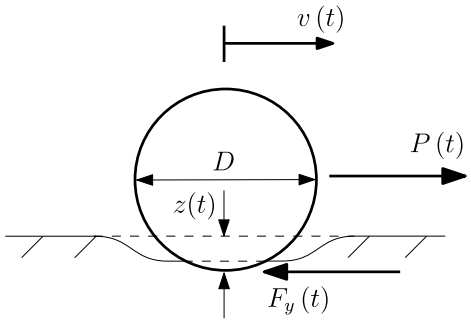

Fig. 5. Pipe–soil verification model.

Table 1
Properties of pipe model.

Quantity	Symbol	Value	Unit
Structural mass		98.5	$\mathrm{kg\,m^{-1}}$
Submerged weight	w_s	137.5	$\mathrm{N\,m^{-1}}$
External diameter	D	324	mm
Length		2.0	m
Number of elements		1	

3. Results

The new pipe–soil formulation in Section 2 was implemented in the SIMLA software [29] which is a special-purpose 3D finite element software for nonlinear static and dynamic analysis of offshore pipelines. The response of a short pipe section was simulated by using the SIMLA software and the 2D PONDUS software, see Table 1 and Fig. 5. The analysis was performed by applying gravity and external pressure in static mode. Thereafter, the analysis was restarted in dynamic mode at time $t_0 = 1.0\,\mathrm{s}$ with the pipe subjected to the following sinusoidal distributed load in the lateral direction,

$$P(t) = P_a \sin\left(\frac{2\pi\,(t - t_0)}{T}\right) \qquad t_0 = 1.0\,\mathrm{s} \qquad T = 6.0\,\mathrm{s} \tag{82}$$

where the load amplitude P_a was set to cover displacements in the elastic range, the pre-breakout region and the post-breakout region. The hydrodynamic mass and drag loads were set equal to zero for simplicity. The pipe section will displace as a rigid body when subjected to the external loading in Eq. (82). Thus, any potential differences related to the beam formulations in the two kinds of software will not affect the simulated results.

3.1. Clay

The soil parameters used in the simulations are listed in Table 2. The initial soil penetration $z(t_0)$ and the residual penetration z_3 were both equal to $8.54\,\mathrm{mm}$, resulting in the following initial yield force curve coordinates,

$$F_{Y1} = 19.91\,\mathrm{N\,m^{-1}}$$
$$F_{Y2} = 19.91\,\mathrm{N\,m^{-1}}$$
$$F_{Y3} = 19.91\,\mathrm{N\,m^{-1}}$$
$$v_{p1} = 0.0\,\mathrm{m}$$
$$v_{p2} = 0.24\,\mathrm{m}$$
$$v_{p3} = 0.58\,\mathrm{m}$$
$$v_{p4} = -0.24\,\mathrm{m}$$
$$v_{p5} = -0.58\,\mathrm{m}$$

The numerical performance in the pre-breakout range was studied by using a load amplitude $P_a = 65\,\mathrm{N\,m^{-1}}$. The total pipe–soil force in Fig. 6 is seen to increase monotonously prior to the load reversal, indicating that the breakout resistance is not reached. The displacement and soil penetrations from PONDUS follow the predictions by SIMLA within an acceptable tolerance, see Figs. 7 and 8. Although some deviations do occur for the PONDUS simulation with $\Delta t = 0.1\,\mathrm{s}$, the predictions are overall in line with SIMLA. Observe that the pipe–soil force in Fig. 6 contains significant oscillations. This is because the simulations were performed with very low damping to ensure correct comparison between PONDUS and SIMLA. The oscillations would disappear if a realistic damping level was applied.

Table 2
Properties of clay.

Quantity	Symbol	Value	Unit
Elastic stiffness	k	65 000	$\mathrm{N\,m^{-2}}$
Dry unit weight	γ_d	18 000	$\mathrm{N\,m^{-3}}$
Submerged unit weight	γ_s	7945	$\mathrm{N\,m^{-3}}$
Unit weight of water	γ_w	10 055	$\mathrm{N\,m^{-3}}$
Undrained shear strength	s_u	800	$\mathrm{N\,m^{-2}}$
Friction coefficient	μ	0.2	

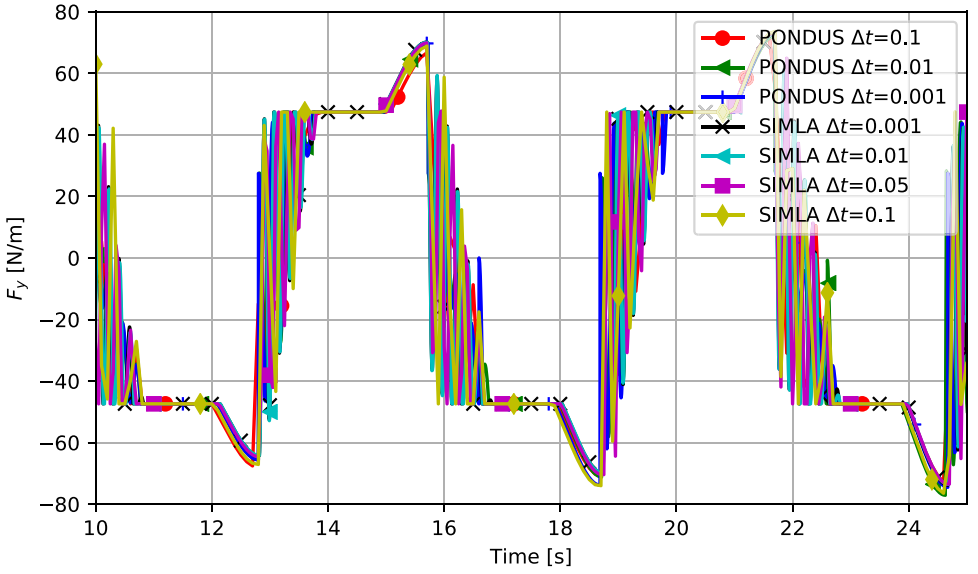

Fig. 6. Total pipe–soil force in lateral direction, clay, F_a =65 N m^{-1}, T =6 s.

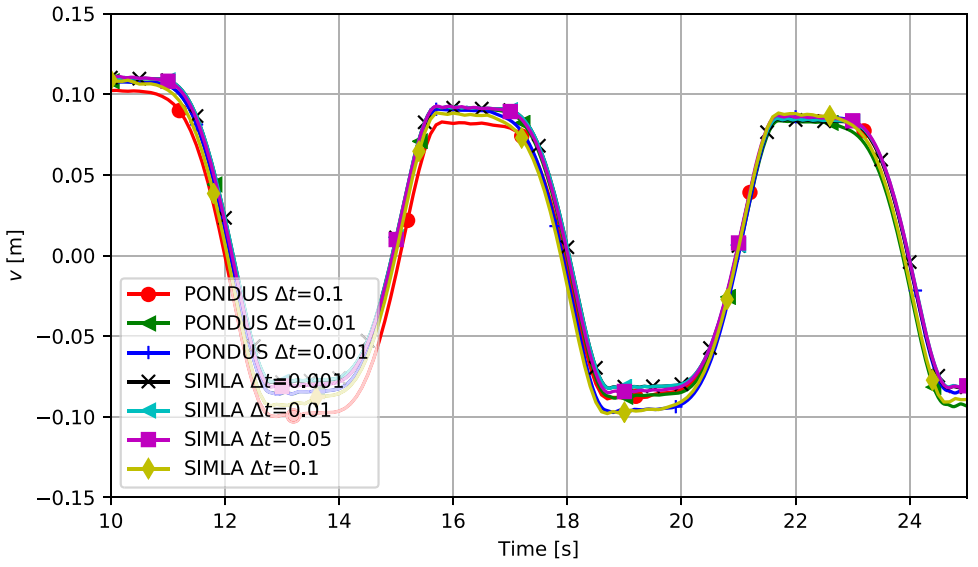

Fig. 7. Displacement in lateral direction, clay, F_a =65 N m^{-1}, T =6 s.

Simulations were conducted for $P_a = 100\,\mathrm{N\,m^{-1}}$ to study the numerical performance in the post-breakout range. The converged maximum lateral displacement is approximately 1.0 m, see Fig. 10. The SIMLA displacements and penetrations agree fairly well for time steps $\Delta t \leq 0.05$ s, see Figs. 10 and 11. SIMLA deviates significantly from the other simulations for $\Delta t = 0.1$ s, implying that $\Delta t = 0.05$ s appears to be the limiting time step size for convergence. The PONDUS simulation for $\Delta t = 0.1$ s agrees well with SIMLA in

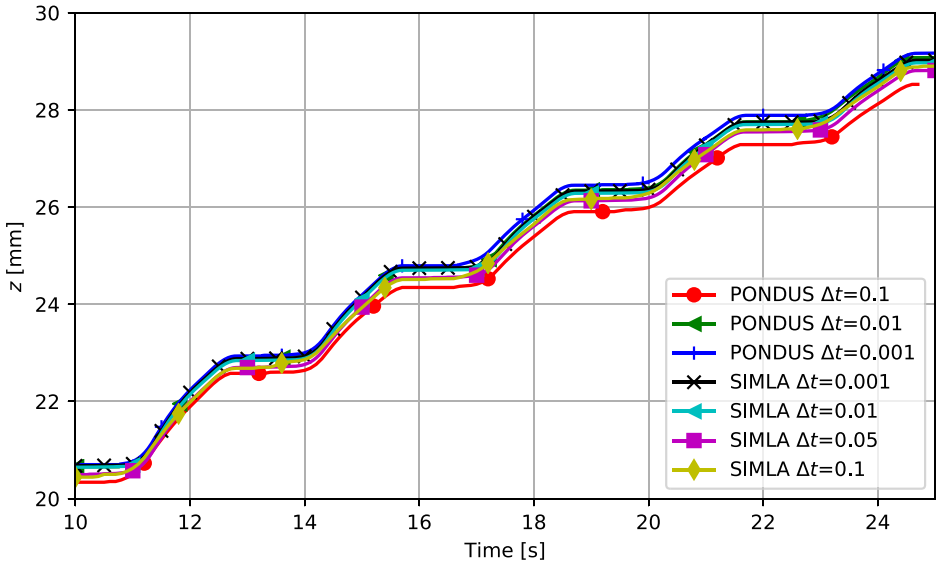

Fig. 8. Penetration development, clay, F_a =65 N m^{-1}, T =6 s.

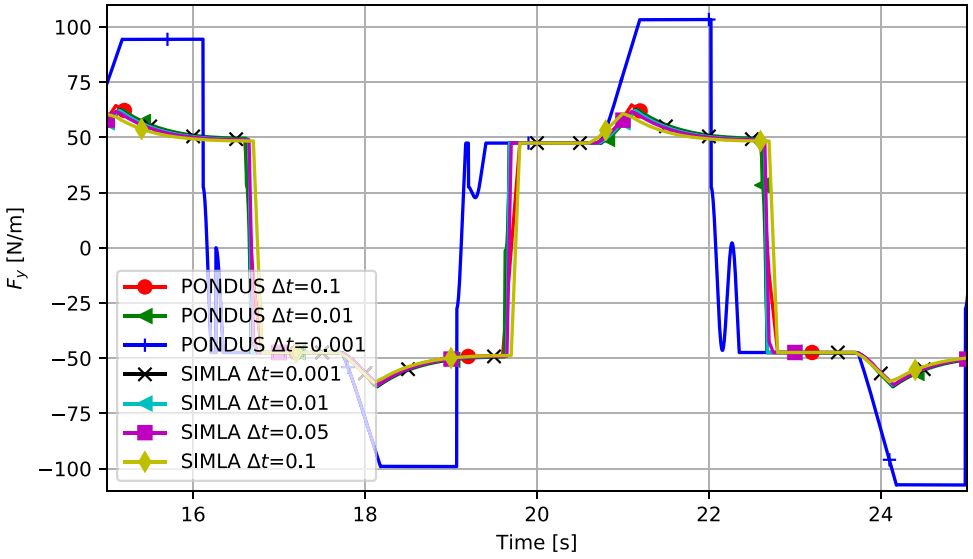

Fig. 9. Total pipe–soil force in lateral direction, clay, P_a =100 N m^{-1}.

terms of lateral displacement, see Fig. 10. PONDUS is however seen to deviate more when the time step size is reduced to Δt=0.01 s, see Fig. 10. Surprisingly, the PONDUS simulation for Δt = 0.001 s gives completely wrong predictions for the total pipe–soil force, the lateral displacement and the soil penetration, see Figs. 9–11. This demonstrates that the PONDUS pipe–soil algorithm has a time step sensitivity issue that prevents monotonous convergence to the correct solution when the time step size is reduced.

Simulations were conducted for P_a = 325 N m^{-1} to check the numerical performance for large lateral displacements up to 25 m, see Fig. 13. Equilibrium is here governed by inertia forces instead of pipe–soil interaction forces, which is seen by comparing the 325 N m^{-1} external load with the maximum pipe–soil force of 60 N m^{-1} in Fig. 12. This implies that the selected example is not a strict test for the pipe–soil algorithm. The lateral displacements from SIMLA and the PONDUS simulation with Δt = 0.01 s coincide throughout the simulation, see Fig. 13. The lateral displacement history for the PONDUS simulation with Δt = 0.1 s deviates significantly, and surprisingly also the PONDUS simulation with Δt = 0.001 s deviates a little, see Fig. 13. The deviations in PONDUS for Δt = 0.1 s and Δt = 0.001 s are further confirmed by the soil penetration time history in Fig. 14.

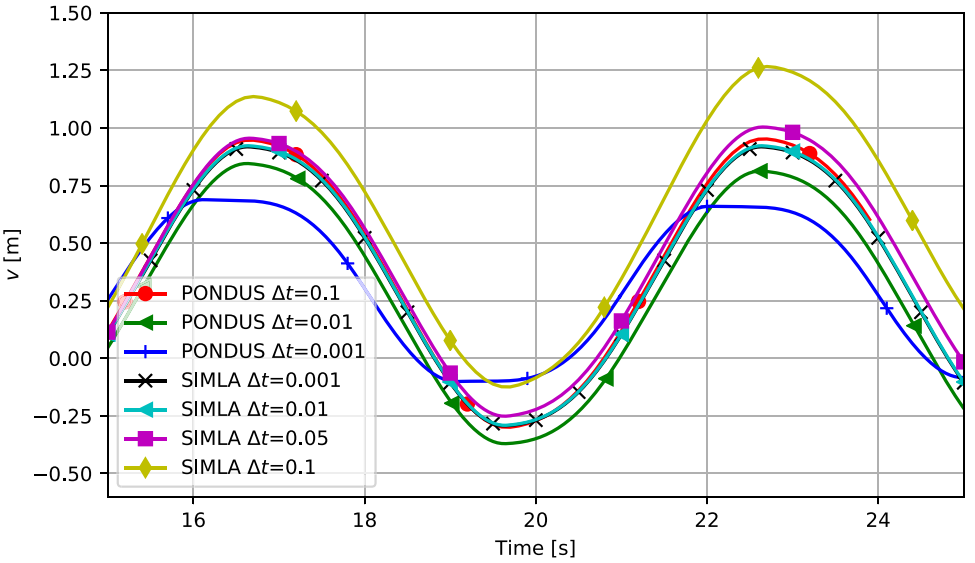

Fig. 10. Displacement in lateral direction, clay, $P_a = 100\,\mathrm{N\,m^{-1}}$.

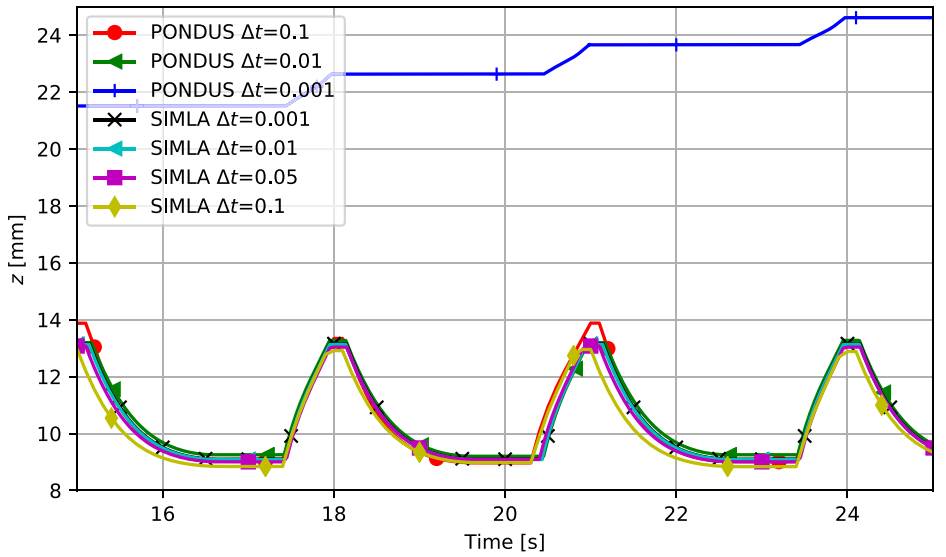

Fig. 11. Penetration development, clay, $P_a = 100\,\mathrm{N\,m^{-1}}$.

3.2. Sand

The soil parameters used in the simulations are listed in Table 3. The initial soil penetration $z(t_0)$ was 9.7 mm and the residual penetration z_3 was 7.0 mm, resulting in the following initial yield force curve coordinates,

$$F_{Y1} = 3.38\,\mathrm{N\,m^{-1}}$$
$$F_{Y2} = 11.28\,\mathrm{N\,m^{-1}}$$
$$F_{Y3} = 7.53\,\mathrm{N\,m^{-1}}$$
$$v_{p1} = 0.0\,\mathrm{m}$$
$$v_{p2} = 0.032\,\mathrm{m}$$
$$v_{p3} = 0.097\,\mathrm{m}$$
$$v_{p4} = -0.032\,\mathrm{m}$$
$$v_{p5} = -0.097\,\mathrm{m}$$

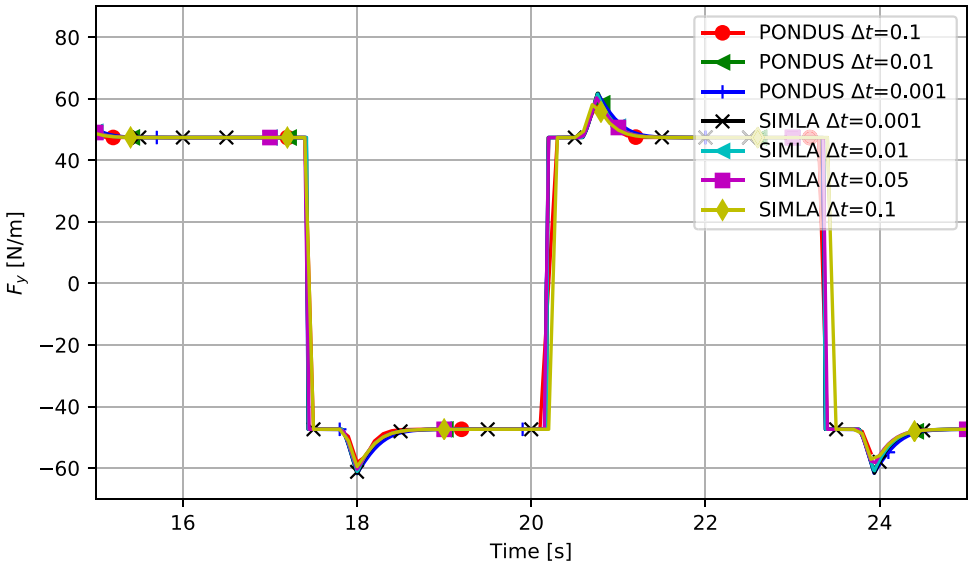

Fig. 12. Total pipe–soil force in lateral direction, clay, P_a =325 N m^{-1}.

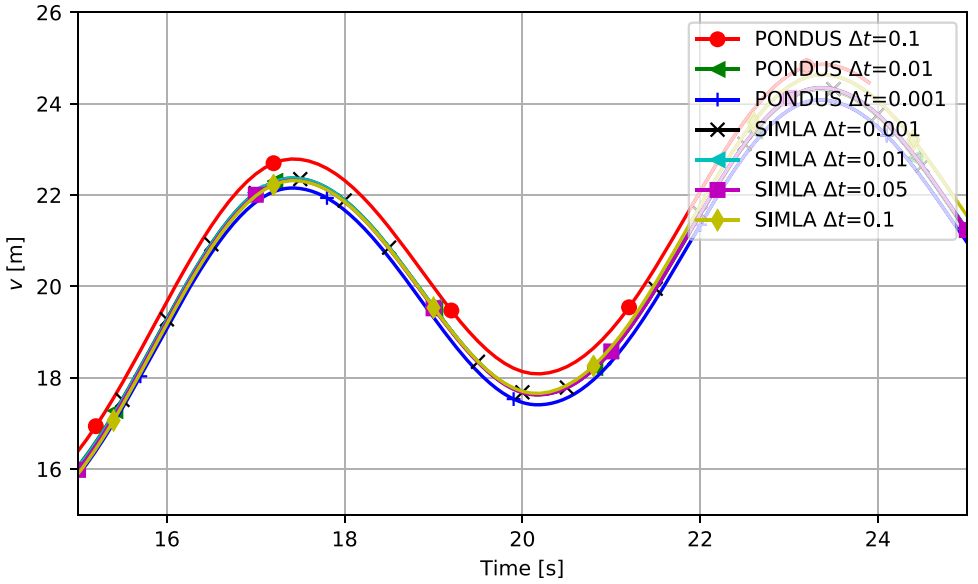

Fig. 13. Displacement in lateral direction, clay, P_a =325 N m^{-1}.

Table 3
Properties of sand.

Quantity	Symbol	Value	Unit
Elastic stiffness	k	65 000	N m^{-2}
Submerged unit weight	γ_s	1800	N m^{-3}
Unit weight of water	γ_w	10 055	N m^{-3}
Dry unit weight	γ_d	11 855	N m^{-3}
Friction coefficient	μ	0.6	

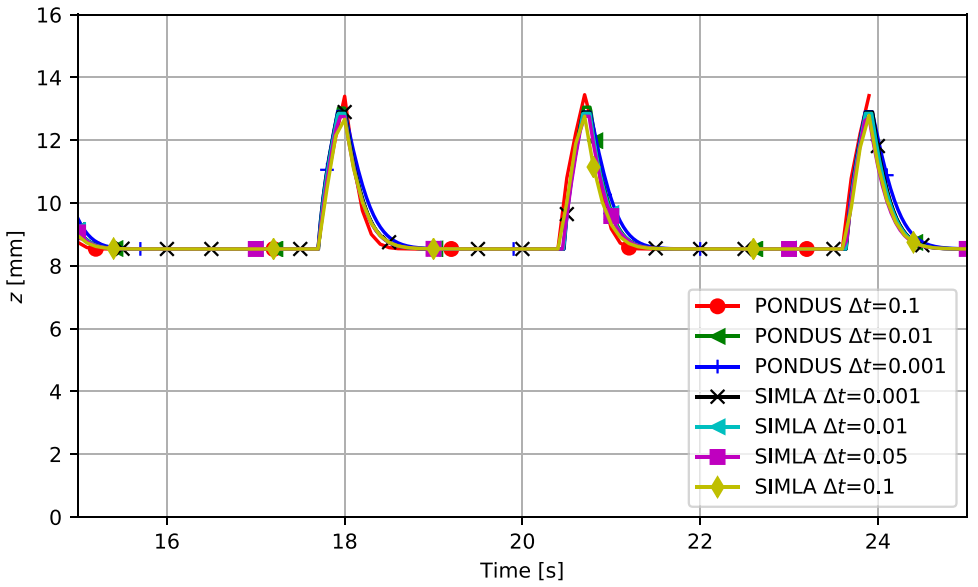

Fig. 14. Penetration development, clay, P_a =325 N m^{-1}.

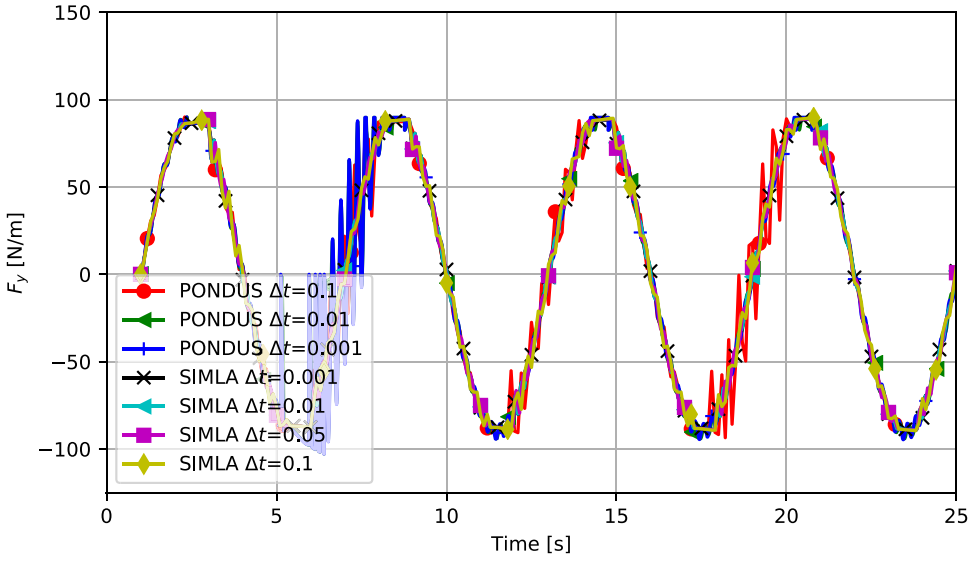

Fig. 15. Total pipe–soil force in lateral direction, sand, F_a =90 N m^{-1}.

A load amplitude of $P_a = 90\,\mathrm{N\,m^{-1}}$ was applied to study the performance for small lateral displacements. The pipe–soil forces are in good agreement for all of the SIMLA and PONDUS simulations regardless of the time step size, see Fig. 15. The lateral displacements predicted by SIMLA are more or less coincident for all the considered time steps Δt from 0.001 s to 0.1 s, see Fig. 16.

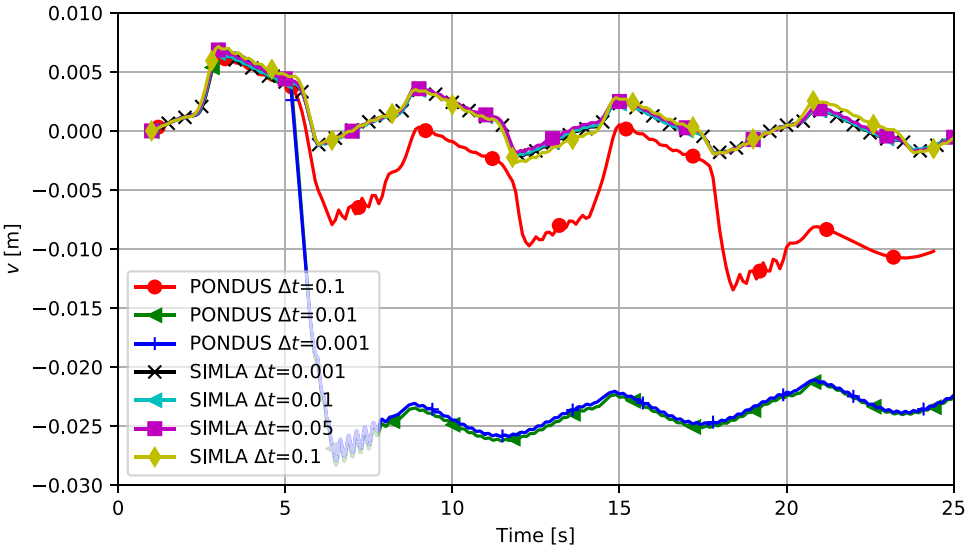

Fig. 16. Displacement in lateral direction, sand, F_a =90 N m^{-1}.

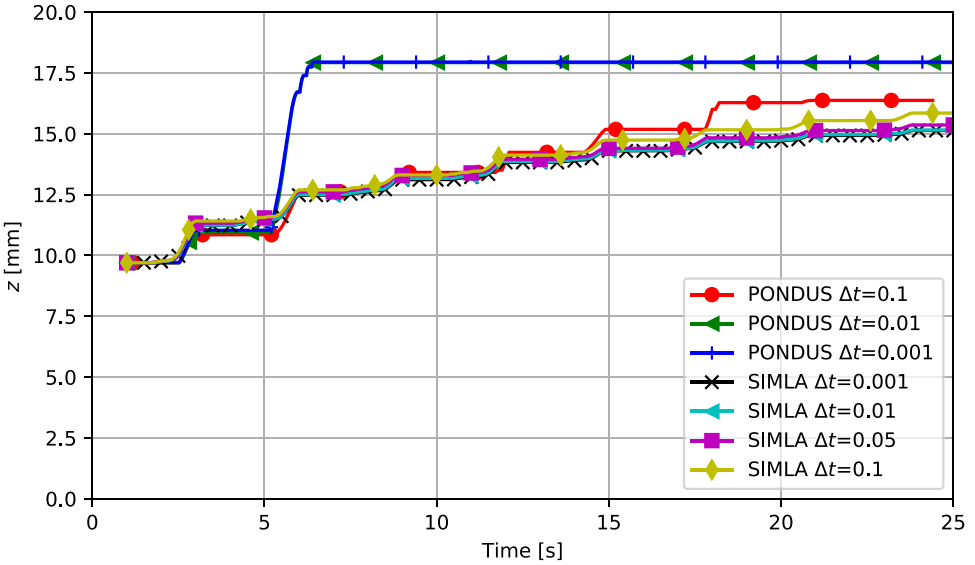

Fig. 17. Penetration development, sand, F_a =90 N m^{-1}.

In contrast, PONDUS predicts wrong lateral displacements with a significant offset from the correct solution for all time steps, and the deviations increase as the time step is reduced, see Fig. 16. The poor performance of PONDUS is further confirmed by the large deviations present for the soil penetrations in Fig. 17. Here, the SIMLA penetration for Δt=0.1 s is seen to deviate slightly from the other SIMLA runs.

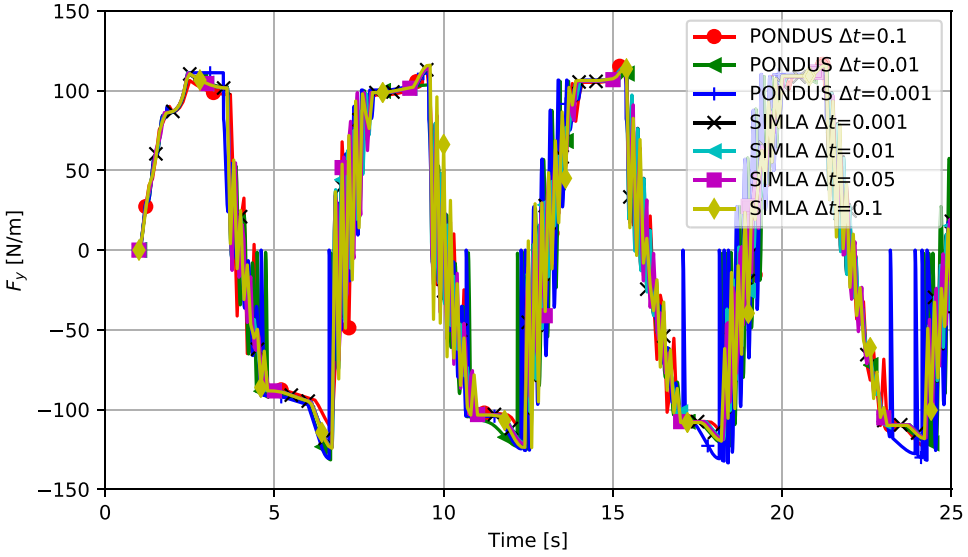

Fig. 18. Total pipe–soil force in lateral direction, sand, $P_a = 120\,\mathrm{N\,m^{-1}}$.

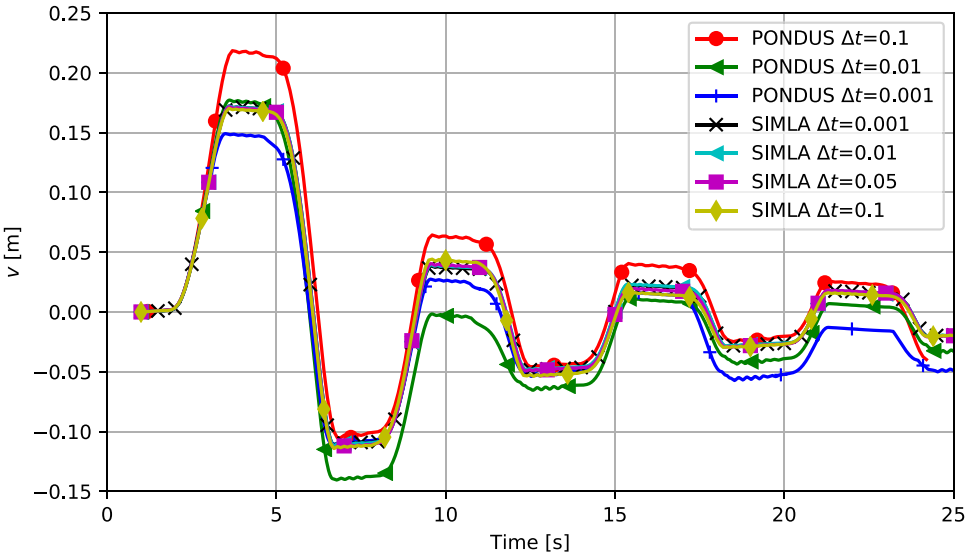

Fig. 19. Displacement in lateral direction, sand, $P_a = 120\,\mathrm{N\,m^{-1}}$.

The performance in the pre-breakout range up to approximately 0.2 m displacement was studied by using a load amplitude $P_a = 120\,\mathrm{N\,m^{-1}}$. 20. The soil penetrations and lateral displacements in SIMLA are coincident up to $\Delta t < 0.05$ s, and a minor deviation occurs for $\Delta t = 0.1$ s, see Figs. 19 and 20. In contrast, the lateral displacement histories predicted by PONDUS deviate by up to 0.05 m compared to SIMLA, see Fig. 19. The PONDUS soil penetration for time step $\Delta t = 0.01$ s is almost in agreement with SIMLA, see

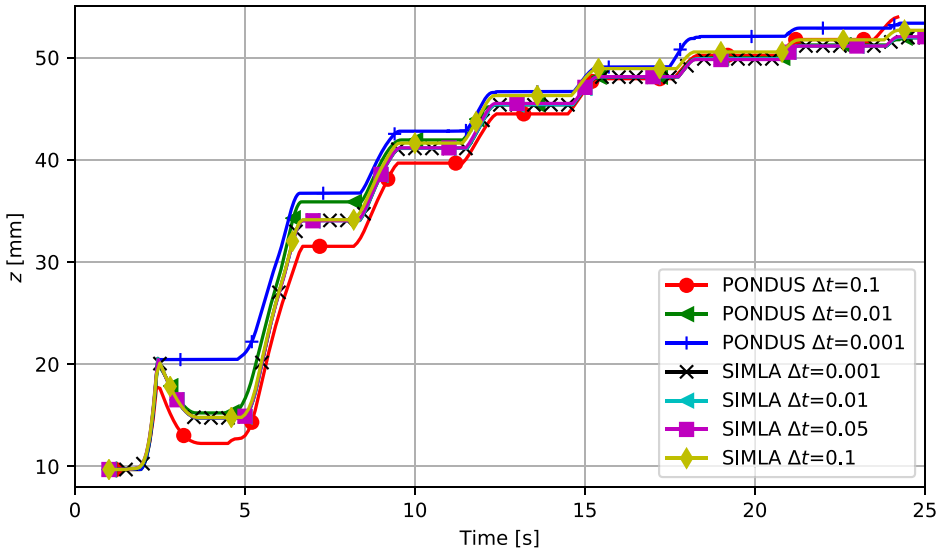

Fig. 20. Penetration development, sand, $P_a = 120\,\mathrm{N\,m^{-1}}$.

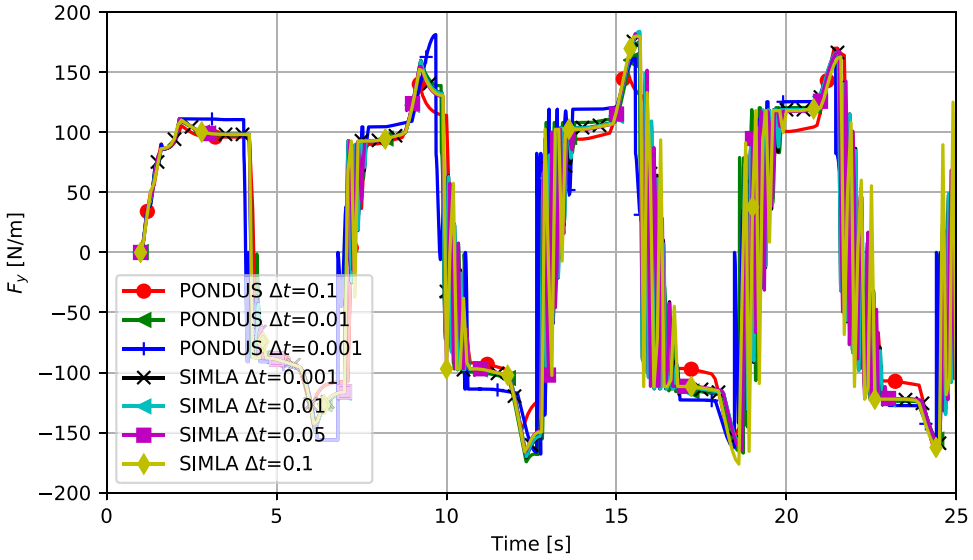

Fig. 21. Total pipe–soil force in lateral direction, sand, $P_a = 150\,\mathrm{N\,m^{-1}}$.

Fig. 20, but larger deviations are present for $\Delta t = 0.1$ s and $\Delta t = 0.001$ s. The deviations for the soil penetrations and the displacements show that PONDUS does not necessarily converge to the correct solution when the time step size is reduced. The elastic oscillations present in the force histories in Fig. 18 occur because the simulations had very low damping to ensure correct comparison between PONDUS and SIMLA. The oscillations would disappear if a larger damping level was applied.

The performance of the sand model in the post-breakout range with lateral displacements up to 0.8 m was studied for $P_a = 150\,\mathrm{N\,m^{-1}}$. Similar to $P_a = 120\,\mathrm{N\,m^{-1}}$, SIMLA predicts displacements that are nearly coincident for time steps $\Delta t \leq 0.05$ s and small deviations are present for $\Delta t = 0.1$ s, see Fig. 22. The soil penetrations predicted by SIMLA are coincident for $\Delta t \leq 0.01$ s and deviate slightly for $\Delta t = 0.05$ s and $\Delta t = 0.1$ s, see Fig. 23. The PONDUS response for $\Delta t = 0.01$ s deviates only slightly from SIMLA. Larger deviations are present for the PONDUS pipe–soil forces, displacements and soil penetrations for time steps of $\Delta t = 0.1$ s and $\Delta t = 0.001$ s, see Figs. 21–23. The large deviations and the failure to converge to the correct solution for $\Delta t = 0.001$ s confirm the poor numerical performance of PONDUS.

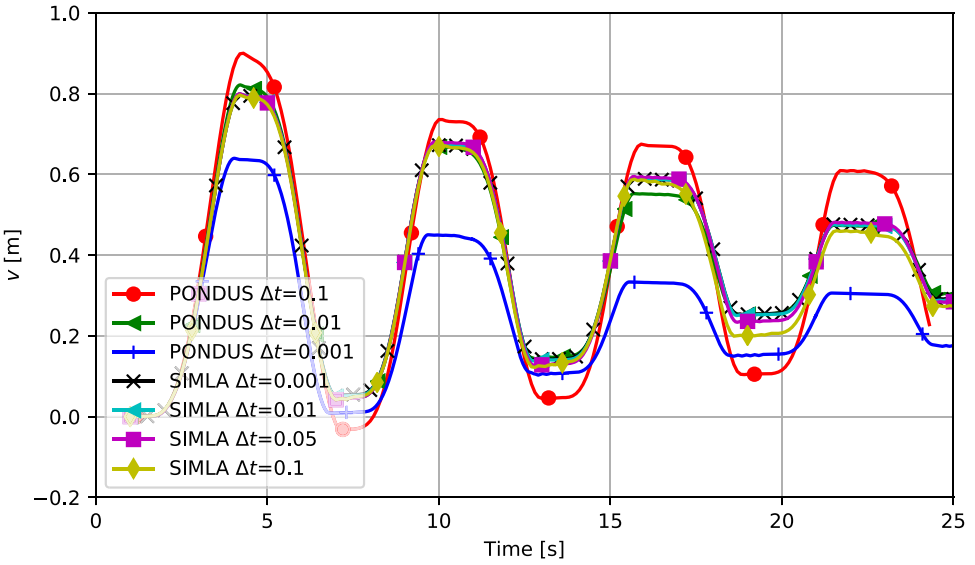

Fig. 22. Displacement in lateral direction, sand, P_a =150 N m^{-1}.

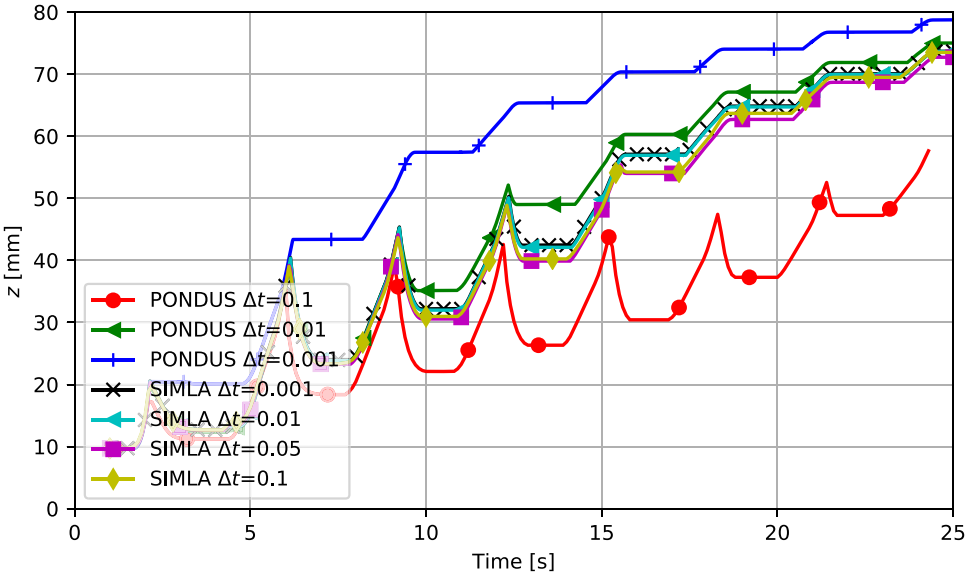

Fig. 23. Penetration development, sand, P_a =150 N m^{-1}.

4. Conclusions

This work contributes with new, robust and effective formulations for the pipe–soil interaction models developed by Verley and Lund for clay and by Verley and Sotberg for sand. Several weak points of the original formulation implemented in the PONDUS software were identified. The weak points were used as basis for developing a backward-Euler force update algorithm. The force updating was optimized by utilizing a closed-form solution for the yield force in the post break-out phase and sub-incrementation prior to break-out. The new pipe–soil formulation was implemented in the SIMLA software, and the improved performance was documented by a numerical comparison study against the PONDUS software.

A significant enhancement of the numerical efficiency was achieved in the present work. The simulated results show that the developed pipe–soil formulation allows for a time step size of up to 0.05 s. In contrast, the PONDUS user manual [30] states that the time step size must be limited to 0.01 s for sand and to 0.001 s for clay. For the resembling PILS software [2] the recommended time step is 0.001 s regardless of the soil type. Hence, the time step size in SIMLA can be increased by a factor of up to 50 times

compared to existing commercial software. This represents a major improvement which is especially beneficial for long-duration 3D nonlinear time domain analysis where the computational cost per time step is significant.

The responses predicted by PONDUS were shown to be very sensitive to the time step size and did not necessarily converge monotonously to the correct solution when the step size was reduced. Such robustness issues are avoided with the new pipe–soil formulation.

The main reasons for the improved numerical performance can be summarized by:

- A fully implicit backward-Euler integration scheme is applied for the force update algorithm. This integration scheme has superior numerical stability properties, and allows for significantly larger time steps. Also, drift-off from the correct solution is avoided since the yield criterion is enforced at the end of the time step.
- The force update is performed by an algorithm that can be linearized to obtain the tangent stiffness for the global Newton–Raphson solution procedure.
- The subincrementation in Section 2.8.1 is an attractive technique for ensuring high accuracy for large time step sizes during the pre-breakout phase. Moreover, for long pipeline models, the cost of subincrementation is less than the cost of performing the analysis with small time steps, and consequently the CPU time will reduce.
- The closed-form solution in Section 2.8.2 enables use of large time steps during the post-breakout phase. Without this feature, much smaller time steps would be necessary in order to capture the continuous change of the plastic modulus H_{v_p}.

Declaration of competing interest

The authors declare that they have no known competing financial interests or personal relationships that could have appeared to influence the work reported in this paper.

Acknowledgments

The authors would like to thank the DROPS JIP sponsors for permission to publish this paper. The first phase of the DROPS JIP is sponsored by CNOOC, Equinor, Norske Shell, IKM Ocean Design, Aker Solutions, Saipem, Gassco, Subsea 7 Norway and Alcatel Submarine Networks Marine.

References

[1] Gagliano M. Offshore pipeline stability during major storm events (https://primis.phmsa.dot.gov/rd/mtgs/020707/mannygagliano.pdf). 2007.
[2] Sollund H, Vedeld K, Grandal JP, Bergan-Haavik J. Pipeline lateral stability software - Technical manual. Tech. rep. 2016-1047, Rev. 0, DNV GL, Høvik, Norway; 2017.
[3] Sotberg T, Holthe K, Lund KM, Igland RT. PONDUS technical manual revised. Tech. rep. STF70 F94034 R, SINTEF Structures and Concrete, Trondheim, Norway; 1994.
[4] Recommended practice DNV-RP-F105, Free spanning pipelines, June 2017. Det Norske Veritas, Høvik, Norway; 2017.
[5] Recommended practice DNV-RP-F109, On-bottom stability design of submarine pipelines, May 2017. Det Norske Veritas, Høvik, Norway; 2017.
[6] Recommended practice DNV-RP-F110, Global buckling of submarine pipelines, September 2019. Det Norske Veritas, Høvik, Norway; 2019.
[7] Sorenson T, Bryndum MB, Jacobsen V. Hydrodynamic forces on pipelines - Model tests. Tech. rep. L51522e, Danish Hydraulic Institute; 1986.
[8] Thorsen MJ, Sævik S, Larsen CM. Time domain simulation of vortex-induced vibrations in stationary and oscillating flow. J Fluid Struct 2016;61:1–19.
[9] Palmer AC. A flaw in the conventional approach to stability design of pipelines. In: Proceedings of the offshore pipeline technology conference. OPT; 1996.
[10] Draper S, Griffiths T, Cheng L, White D, An H. Modelling changes to submarine pipeline embedment and stability due to pipeline scour, OMAE2018-77985. In: Proceedings of the ASME 2018 37th international conference on ocean, offshore and arctic engineering. ASME; 2018.
[11] Brennodden H, Sveggen O, Wagner DA, Murff JD. Full-scale pipe-soil interaction tests. In: 18th annual OTC in Houston. Offshore Technology Conference; 1986, p. 433–40.
[12] Brennodden H. Pipe-soil interaction tests on sand and soft clay. Report STF69 F887018, prepared for the American Gas Association, SINTEF; 1988.
[13] Allen D, Lammert WF, Hale JR, Jacobsen V. Submarine pipeline on-bottom stability: Recent AGA research. In: 21st annual OTC in Houston. Offshore Technology Conference; 1989, p. 121–32.
[14] Palmer AC, Steenfelt JS, Steensen-Bach JO, Jacobsen V. Lateral resistance of marine pipelines on sand. In: Proceedings of 20th annual offshore technology conference. OTC; 1988, p. 399–408.
[15] Wagner DA, Murff JD, Brennodden H, Sveggen O. Pipe-soil interaction model. In: 19th annual OTC in Houston. Offshore Technology Conference; 1987, p. 181–90.
[16] Brennodden H, Lieng JT, Sotberg T, Verley RLP. An energy-based pipe-soil interaction model. In: 21st annual OTC in Houston. Offshore Technology Conference; 1989, p. 147–58.
[17] Verley RLP, Reed K. Response of pipeline on various soils for realistic hydrodynamic loading. In: Proceedings of the 8th offshore mechanics and polar engineering conference. ISOPE; 1989, p. 149–56.
[18] Verley RLP, Sotberg T, Brennodden H. Break-out soil resistance for a pipeline partially buried in sand. In: Proceedings of the 9th international conference on offshore mechanics and arctic engineering. ASME; 1990, p. 121–6.
[19] Verley RLP, Sotberg T. A soil resistance model for pipelines placed on sandy soils. In: Proceedings of the 11th international conference on offshore mechanics and arctic engineering. ASME; 1992, p. 123–31.
[20] Verley RLP, Sotberg T. A soil resistance model for pipelines placed on sandy soils. J Offshore Mech Arct Eng 1994;116:145–53.
[21] Verley R, Lund KM. A soil resistance model for pipelines placed on clay soils. In: Proceedings of the 14th international conference on offshore mechanics and arctic engineering. ASME; 1995, p. 225–32.
[22] Abdolmaleki K, Gregory JC. Performance of pipe-soil interaction models in a quasi-dynamic approach to pipeline stability analysis, OMAE2018-77988. In: Proceedings of the ASME 2018 37th international conference on ocean, offshore and arctic engineering. ASME; 2018.

[23] Griffiths T, Draper S, White D, Cheng L, An H, Tong F, et al. Pipeline and cable stability: Updated state of the art, OMAE2018-77736. In: Proceedings of the ASME 2018 37th international conference on ocean, offshore and arctic engineering. ASME; 2018.
[24] Holthe K. PONDUS - Verification examples. Tech. rep. STF71 F85035, SINTEF, Trondheim, Norway; 1985.
[25] Holthe K, Sotberg T, Stavnes B. PONDUS - Maintenance manual. Tech. rep. STF71 F86057, SINTEF, Trondheim, Norway; 1986.
[26] Simo JC, Taylor RL. Consistent tangent operators for rate-independent elastoplasticity. Comput Methods Appl Mech Engrg 1985;48:101–18.
[27] Vedeld K, Sollund H, Grandal JP, Bergan-Haavik J. Subsea pipeline and cable soil resistance models. Tech. rep. 2016-1046, Rev. 0, DNV GL; 2016.
[28] Lieng JT, Sotberg T, Brennodden H. Energy based pipe-soil interaction models. Tech. rep. Report STF69 F87024, prepared for the American Gas Association, SINTEF; 1988.
[29] Sævik S. SIMLA - Theory manual. Tech. rep. 700254.00.01, SINTEF Ocean, Trondheim, Norway; 2017.
[30] Igland RT, Sotberg T, Holthe K, Lund KM. PONDUS user manual. Tech. rep. MT70 F04 235, SINTEF, Trondheim, Norway; 2005.